AIP | Review of Scientific Instruments

# The magnetic recoil spectrometer for measurements of the absolute neutron spectrum at OMEGA and the NIF

D. T. Casey, J. A. Frenje, M. Gatu Johnson, F. H. Séguin, C. K. Li et al.

Citation: Rev. Sci. Instrum. **84**, 043506 (2013); doi: 10.1063/1.4796042
View online: http://dx.doi.org/10.1063/1.4796042
View Table of Contents: http://rsi.aip.org/resource/1/RSINAK/v84/i4
Published by the American Institute of Physics.

# The magnetic recoil spectrometer for measurements of the absolute neutron spectrum at OMEGA and the NIF

D. T. Casey,[1,a)] J. A. Frenje,[1] M. Gatu Johnson,[1] F. H. Séguin,[1] C. K. Li,[1] R. D. Petrasso,[1,b)] V. Yu. Glebov,[2] J. Katz,[2] J. Magoon,[2] D. D. Meyerhofer,[2,c)] T. C. Sangster,[2] M. Shoup,[2] J. Ulreich,[2] R. C. Ashabranner,[3] R. M. Bionta,[3] A. C. Carpenter,[3] B. Felker,[3] H. Y. Khater,[3] S. LePape,[3] A. MacKinnon,[3] M. A. McKernan,[3] M. Moran,[3] J. R. Rygg,[3] M. F. Yeoman,[3] R. Zacharias,[3] R. J. Leeper,[4] K. Fletcher,[5] M. Farrell,[6] D. Jasion,[6] J. Kilkenny,[6] and R. Paguio[6]

[1]*Plasma Science and Fusion Center, Massachusetts Institute of Technology, Cambridge, Massachusetts 02139, USA*
[2]*Laboratory for Laser Energetics, University of Rochester, Rochester, New York 14623, USA*
[3]*Lawrence Livermore National Laboratory, Livermore, California 94550, USA*
[4]*Sandia National Laboratories, Albuquerque, New Mexico 87185, USA*
[5]*State University of New York Geneseo, Geneseo, New York 14454, USA*
[6]*General Atomics, San Diego, California 92186, USA*

(Received 2 October 2012; accepted 7 March 2013; published online 18 April 2013)

The neutron spectrum produced by deuterium-tritium (DT) inertial confinement fusion implosions contains a wealth of information about implosion performance including the DT yield, ion-temperature, and areal-density. The Magnetic Recoil Spectrometer (MRS) has been used at both the OMEGA laser facility and the National Ignition Facility (NIF) to measure the absolute neutron spectrum from 3 to 30 MeV at OMEGA and 3 to 36 MeV at the NIF. These measurements have been used to diagnose the performance of cryogenic target implosions to unprecedented accuracy. Interpretation of MRS data requires a detailed understanding of the MRS response and background. This paper describes *ab initio* characterization of the system involving Monte Carlo simulations of the MRS response in addition to the commission experiments for *in situ* calibration of the systems on OMEGA and the NIF. © *2013 American Institute of Physics*. [http://dx.doi.org/10.1063/1.4796042]

## I. INTRODUCTION

In inertial confinement fusion (ICF) experiments performed at the OMEGA laser facility[1] and the National Ignition Facility (NIF),[2] capsules filled with deuterium and tritium (DT) are imploded to extraordinary temperatures and pressures with the goal of initiating thermonuclear burn. The DT neutron spectrum, produced by these experiments, contains a wealth of information vital for evaluating implosion performance. Many essential implosion metrics, including areal-density ($\rho$R), ion temperature ($T_i$), and neutron yield ($Y_n$), are inferred from the neutron spectrum. The Magnetic Recoil Spectrometer (MRS)[3] was developed and commissioned on OMEGA in 2007 and on the NIF in 2010 for measurements of the neutron spectrum, produced by high-$\rho$R implosions (>0.18 g/cm$^2$) that are not accessible by charged-particle techniques.[4,5]

This paper is organized as follows: Sec. II discusses the MRS principle. Sec. III presents the final design of the MRS on both OMEGA and the NIF. Section IV reviews the characterization of the MRS parameters important for determining response. Section V discusses the *ab initio* modeling of the MRS-response function and *in situ* calibration of the installed systems. Section VI presents the complete MRS-response function simulated with the code Geant4.[6] Section VII elaborates on the modeling of the neutron-background and optimal shielding design for the MRS on both OMEGA and the NIF. Section VIII applies the MRS technique to diagnose cryogenic DT implosions at OMEGA and NIF, while Sec. IX summarizes the paper.

## II. PRINCIPLE

The MRS is a neutron spectrometer that utilizes neutron-to-deuteron (or proton) elastic scattering and magnetic dispersion of the recoil deuterons (or protons).[3] This implementation is similar to a wide variety of spectrometry applications, such as in accelerator and tokamak experiments.[3,7] The first design study of the MRS for ICF experiments was published in 2001 by Frenje *et al.*[3] There, the MRS concept was discussed for the measurement of the ICF neutron spectrum, from which $\rho$R, $T_i$, and $Y_n$ can be determined. The MRS consists of three main components (Figure 1). The first component is a $CD_2$ (or $CH_2$) foil positioned at 10 cm and 26 cm from the implosion at OMEGA and the NIF, respectively. The second is a focusing magnet that is located outside the target chamber, and the third is an array of CR-39 detectors positioned at the focal plane of the spectrometer.

The principle of the system is that a small fraction of the neutrons emitted from the implosion hit the $CD_2$ ($CH_2$) foil producing scattered recoil deuterons (protons). The energy

[a)]Present address: Lawrence Livermore National Laboratory, Livermore, California 94551, USA.
[b)]Also Visiting Senior Scientist at LLE.
[c)]Also at Departments of Mechanical Engineering and Physics and Astronomy.

 

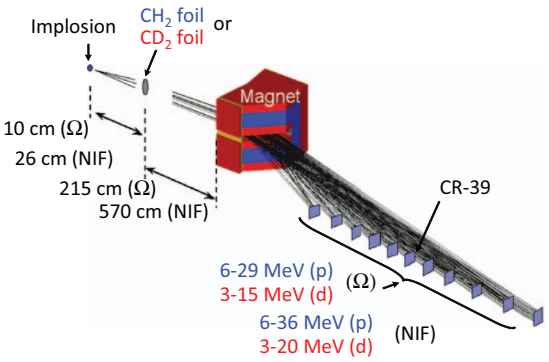


FIG. 1. A schematic drawing of the MRS and its main components: a $CH_2$ (or $CD_2$) foil, magnet, and an array of CR-39 detectors. The MRS uses a foil positioned 10 cm away from the implosion on OMEGA (and 26 cm on the NIF) to convert incident neutrons to charged recoil particles. The measured recoil-particle spectrum is then used to determine the neutron spectrum from the implosion. Reprinted with permission from J. A. Frenje *et al.*, Phys. Plasmas **17**, 056311 (2010). Copyright 2010 American Institute of Physics.

relationship between the recoil particle ($E_r$) and the neutron ($E_n$) is described by

$$E_r = \frac{4A}{(1+A)^2} E_n \mathrm{Cos}^2\theta_r, \quad (1)$$

where A is the atomic mass number of the recoil particle, and $\theta_r$ is the angle between the direction of the incoming neutron and the direction of the outgoing recoil particle. Recoil protons or deuterons with a scattering angle of $\theta_r \sim 0$ are selected by an aperture, positioned in front of the magnet, which defines the MRS line-of-sight (LOS). The selected recoil particles are energy dispersed by their momentum (or energy) as described by

$$R_G = \frac{p}{qB} = \frac{\sqrt{2mE_r}}{qB}. \quad (2)$$

$R_G$ is the gyro radius, $p$ is the momentum, $q$ is the charge, $m$ is the mass, $E_r$ is the energy of the recoil particle, and $B$ is the MRS magnetic field (perpendicular to the incident particle trajectory). The energy-dispersed particles are then focused onto the detectors. The magnetic dispersion and focusing provides a mapping between position at the detector and energy of the proton or deuteron and thus the energy of the neutron that scattered it. The CR-39 detectors record the position of each recoil particle with a detection efficiency of 100%. By measuring the spectrum of the recoil particles, the neutron spectrum is indirectly measured.

An important characteristic of the MRS is that the detection efficiency [$\varepsilon_{MRS}(E_n)$], for a specified energy resolution [$\Delta E_{MRS}(E_n)$], has been carefully optimized (these parameters are discussed further in the Sec. II B).[3] This is achieved in part because the differential cross sections in the laboratory frame, for elastic np- or nd-scattering peak, in the forward direction and the average path length of the recoil particles in the foil are minimized. In addition, magnetic focusing allows for the largest possible solid angle to be used, maximizing $\varepsilon_{MRS}$ for a specified $\Delta E_{MRS}$ (discussed more in Sec. III C).

### A. Efficiency

The detection efficiency of the MRS is given by

$$\varepsilon_{MRS}(E_n) = \frac{\Omega_n}{4\pi} \cdot T(E_r) \cdot n_i \cdot t \int^{''\Omega_r''} \frac{d\sigma(E_n)}{d\Omega_{lab}} d\Omega, \quad (3)$$

where $\Omega_n$ is the solid angle subtended by the foil, $n_i$ is the number density of deuterons (protons) in the foil, $t$ is the foil thickness, $\Omega_r$ is the solid angle defined by the magnet aperture, $d\sigma(E_n)/d\Omega_{lab}$ is the differential cross section in the laboratory system for elastic scattering, and $T(E_r)$ is the spectrometer transmission function. $T(E_r)$ is used if the particle distribution, perpendicular to the dispersive plane, extends beyond the CR-39 height (see Sec. IV D). For the OMEGA MRS, $T(E_r)$ depends on recoil-particle energy because the CR-39 detectors are further away from the magnet at higher energies. Also $d\sigma(E_n)/d\Omega_{lab}$ depends on the incident neutron energy (see Figure 18). As these parameters are well known, the MRS can be accurately characterized from first principles (*ab initio*), allowing quantitative calculations of the MRS response before the system has been built and installed. This is an important strength of the technique, but an *in situ* energy calibration is, however, required to check that the system has been built and installed according to specification. The *ab initio* characterization and *in situ* calibration experiments of the MRS on OMEGA and the NIF are discussed in Sec. V.

### B. Energy resolution

The MRS energy resolution [$\Delta E_{MRS}(E_n)$] can be approximated by the expression

$$\Delta E_{MRS}(E_n) \approx \sqrt{\Delta E^2_{foil}(E_n) + \Delta E^2_{kin}(E_n) + \Delta E^2_{mag}(E_n)}. \quad (4)$$

$\Delta E_{MRS}(E_n)$ is the total energy resolution, $\Delta E_{foil}(E_n)$ is the energy broadening due to different path lengths in the foil resulting in different energy losses, $\Delta E_{kin}(E_n)$ is the kinematic broadening due to the dependence of the recoil energy on scattering angle $\theta_r$ ($E_r \propto \mathrm{Cos}^2\theta_r$), and $\Delta E_{mag}(E_n)$ is the broadening due to ion-optical aberrations of the magnet. $\Delta E_{foil}(E_n)$ is proportional to the thickness and density of the foil. $\Delta E_{kin}(E_n)$ is proportional to the size of the foil because larger foils allow a larger spread of scattering angles to be selected by the aperture in front of the magnet. $\Delta E_{mag}(E_n)$ is proportional to the size of the foil and magnet aperture because the focusing properties of the magnet are degraded for larger offsets from the central trajectory and larger angular spreads of the recoil particles. This gives the NIF MRS system superior performance (see Sec. V), because the foil (almost the same size as OMEGA) is further away from the magnet aperture, resulting in a much smaller angular spread of the recoil particles. However, this comes at the cost of detection efficiency.

For the MRS to be useful at OMEGA and the NIF, built-in flexibility has been incorporated into the design to effectively use it in different applications. This flexibility allows for a tradeoff between $\varepsilon_{MRS}$ and $\Delta E_{MRS}$. For practical implementation of low-yield applications, such as measurements of down-scattered neutrons (DSn) from OMEGA implosions, where yields are orders of magnitude smaller than the primary yield, it is necessary to degrade $\Delta E_{MRS}$ to

substantially increase $\varepsilon_{MRS}$. For high-yield applications, such as measurements of the primary neutron spectrum at OMEGA and the NIF, the MRS can be configured to operate in a high-resolution mode (low-$\varepsilon_{MRS}$). Several options are available for configuring the MRS. Either a $CH_2$ or $CD_2$ foil can be selected to produce recoil protons or deuterons. The MRS on OMEGA covers a proton energy range of 6–30 MeV and deuteron energy range of 3–15 MeV, while the MRS on the NIF covers a proton energy range of 6–36 MeV and deuteron energy range of 3–18 MeV. Therefore, the energy range covered for neutrons is approximately 6–30 MeV with the $CH_2$ foil (neglecting energy loss in the foil) or 3–17 MeV with the $CD_2$ foil at OMEGA and 6–36 MeV with the $CH_2$ foil and 3–20 with the $CD_2$ foil at the NIF. The detection-range is larger for the $CD_2$ foil on the low energy end due to magnetic dispersion (Eq. (2)) and larger on the high energy end due to the neutron-to-deuteron kinematic down-shift (Eq. (1)). For adjustments of $\varepsilon_{MRS}$ and $\Delta E_{MRS}$, the foil area and thickness are changed. The area of the aperture in front of the magnet can be adjusted as well.

## III. MRS DESIGN ON OMEGA AND THE NIF

The MRS technique was first implemented on OMEGA in 2007[8] and then on the NIF in 2010.[9] The philosophy was first to comprehensively test the technique on OMEGA, and from the experience gained, insightfully design an optimal MRS for the NIF. There were other important reasons for taking this approach. First, the $\rho R$ of both warm gas-filled CH-capsule and cryogenic DT implosions can be inferred from both the MRS and charged-particle spectrometry for moderate $\rho R$ implosions ($\rho R < 180$ mg/cm$^2$) on OMEGA. This allowed for an independent check of the inferred $\rho R$ from the MRS data.[5,10] Second, when the MRS was first constructed at OMEGA there were no other ways to determine cryogenic $\rho R > 180$ mg/cm$^2$.[5,11] Therefore, the MRS brought a required diagnostic to the cryogenic program.[12,13] Since that time, several complementary cryogenic $\rho R$ techniques have been developed at OMEGA[14] and the NIF[9,15,16] using the nTOF technique.

Images of the MRS fully installed on OMEGA and the NIF target chambers are shown in Figure 2. In both images, the diagnostic is fully surrounded by polyethylene shielding

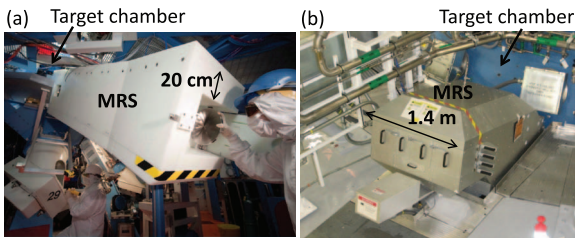


FIG. 2. (a) An image of the OMEGA MRS, surrounded by ~20 cm thick polyethylene shielding. The shielding weighs ~2200 lbs and surrounds the detector housing to reduce the background neutron fluence to the required level for the DSn measurement (photo taken by Eugene Kowaluk). (b) An image of the NIF MRS fully installed on the NIF-target chamber. The MRS detector array is located behind borated gunite target-chamber wall and inside ~6000 lbs of polyethylene shielding, which greatly reduces the background neutron fluence.

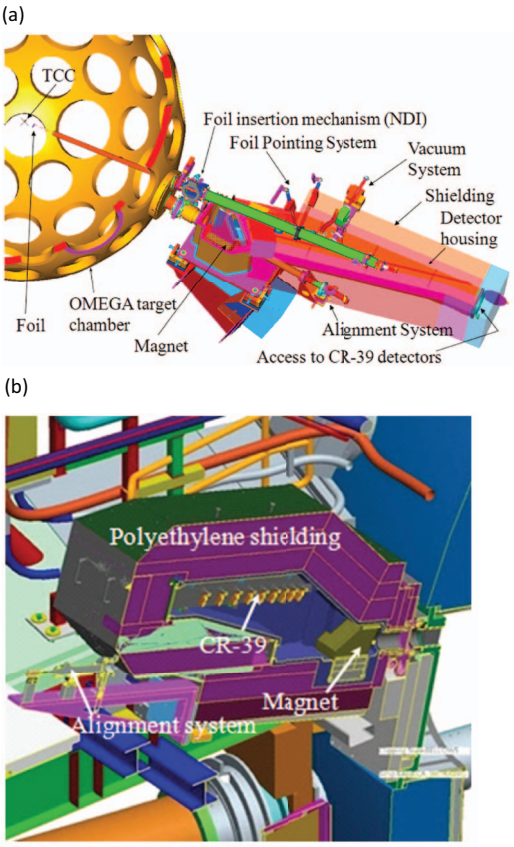


FIG. 3. (a) A CAD drawing of the OMEGA MRS, which is permanently mounted to the OMEGA target chamber. The foil is inserted to a distance of 10 cm from the implosion by the nuclear diagnostic inserter (NDI). The magnet is enclosed by an aluminum vacuum housing, which is connected to the detector vacuum housing. The detector housing is surrounded by ~2200 lbs of polyethylene shielding (shown here as a transparent material). Access to the CR-39 detector array is through the rear door. Reprinted with permission from J. A. Frenje *et al.*, Rev. Sci. Instrum. **79**, 10E502 (2008). Copyright 2008 American Institute of Physics. (b) A CAD drawing of the NIF MRS positioned onto the target chamber at the line-of-sight 77°–324°. A vertical crosscut is made through the MRS to illustrate the various components in the system, i.e., the magnet, CR-39 detector array, alignment system, and shielding. The Diagnostic Insertion Manipulator (DIM) 90°–315°, not shown in this figure, is used to insert the foil to a distance of 26 cm from the implosion. The MRS is fully surrounded by ~6000 lbs of polyethylene shielding and is positioned in the shadow of the 50 cm borated gunite cladding on top of the 10 cm thick aluminum target chamber. Reprinted with permission from J. A. Frenje *et al.*, Phys. Plasmas **17**, 056311 (2010). Copyright 2010 American Institute of Physics.

to suppress the background of primary neutrons and neutrons scattered by the chamber wall, diagnostics, and other structures. In the case of the NIF MRS, grey aluminum plates are attached to the outside shielding to improve fire resistance. Additional neutron shielding is obtained on the NIF by positioning the CR-39 detector array in the shadow of 50 cm of borated gunite, sitting on the 10 cm thick aluminum target chamber. As the CR-39 detector array is positioned on an off-axis detection plane that is well outside the target chamber, enough space exists to position ~2200 lbs and ~6000 lbs of polyethylene shielding around the OMEGA MRS and NIF MRS, respectively. Detailed discussions about shielding-design considerations are presented in Sec. VII.

CAD drawings of the MRS on OMEGA and the NIF are shown in Figure 3. The MRS is permanently attached to the

TABLE I. System parameters for the MRS on OMEGA and the NIF and associated errors.[5] The efficiency and energy resolution for each MRS configuration are also shown.

| Spectrometer parameters | OMEGA High res | OMEGA Med res | OMEGA Low res | NIF High Res | NIF Med Res | NIF Low Res |
|---|---|---|---|---|---|---|
| Foil area ($cm^2$) | $5.7 \pm 0.1$ | $10.6 \pm 0.1$ | $13.2 \pm 0.1$ | $12.8 \pm 0.1$ | $12.8 \pm 0.1$ | $12.8 \pm 0.1$ |
| Foil distance (cm) | $10.3 \pm 0.3$ | $10.3 \pm 0.3$ | $10.5 \pm 0.3$ | $26.0 \pm 0.3$ | $26.0 \pm 0.3$ | $26.0 \pm 0.3$ |
| Foil thickness ($\mu$m) | $62 \pm 1$ | $164 \pm 1$ | $261 \pm 1$ | $47 \pm 1$ | $138 \pm 1$ | $259 \pm 1$ |
| Foil number density ($d/cm^3 \times 10^{22}$) | $7.6 \pm 0.3$ | $7.6 \pm 0.3$ | $7.6 \pm 0.3$ | $7.9 \pm 0.1$ | $7.9 \pm 0.1$ | $7.7 \pm 0.1$ |
| $d\sigma/d\Omega$ (0°) at 14 MeV (b/sr) | $0.50 \pm 0.01$ | $0.50 \pm 0.01$ | $0.50 \pm 0.01$ | $0.50 \pm 0.01$ | $0.50 \pm 0.01$ | $0.50 \pm 0.01$ |
| Magnet distance from foil (cm) | $215 \pm 0.1$ | $215 \pm 0.1$ | $215 \pm 0.1$ | $570 \pm 0.1$ | $570 \pm 0.1$ | $570 \pm 0.1$ |
| Magnet aperture area ($cm^2$) | $21.3 \pm 0.2$ | $21.3 \pm 0.2$ | $21.3 \pm 0.2$ | $20 \pm 0.2$ | $20 \pm 0.2$ | $20 \pm 0.2$ |
| Interception correction | $0.91 \pm 0.01$ | $0.87 \pm 0.01$ | $0.86 \pm 0.01$ | $1 \pm 0$ | $1 \pm 0$ | $1 \pm 0$ |
| Transmission at 14 MeV | $0.83 \pm 0.03$ | $0.79 \pm 0.03$ | $0.79 \pm 0.03$ | $1 \pm 0$ | $1 \pm 0$ | $1 \pm 0$ |
| $\varepsilon_{MRS\ 14\,MeV}$ | $2.72 \times 10^{-10}$ | $1.20 \times 10^{-9}$ | $2.14 \times 10^{-9}$ | $1.56 \times 10^{-11}$ | $4.61 \times 10^{-11}$ | $8.48 \times 10^{-11}$ |
| Total uncertainty at 14 MeV | 8.4% | 8.4% | 8.3% | 4.2% | 4.2% | 4.2% |
| $\Delta E_{MRS}$ FWHM at 14 MeV | 1.0 | 1.3 | 1.8 | 0.69 | 0.80 | 1.6 |

OMEGA target chamber on the 117°–306° port (Figure 3(a)). The foil is inserted by the Nuclear Diagnostic Inserter (NDI). The magnet is surrounded by an aluminum vacuum chamber, which is isolated from the OMEGA target chamber by a gate-valve that allows tritium vent/purge operations to be performed between shots before removal of the CR-39 detector array. The detector housing is connected directly to the magnet chamber and is surrounded by polyethylene shielding. The NIF MRS is permanently attached to the 77°–324° port, which is close to the equator on the NIF target chamber. The foil is inserted to a distance of 26 cm from the implosion by the Diagnostic Insertion Manipulator (DIM) at 90°–315°, which is not shown in this figure. The MRS is positioned close to the edge of the port to take advantage of gunite shielding. The MRS vessel is also positioned between two floor boards (or "diving boards"). Substantial amounts of shielding surround the MRS. Prior to a shot, the CR-39 detector array is inserted into the MRS (see Figure 9). This typically happens an hour to a day before the shot, depending on shot schedule and constraints set by the facility operations. Thirty minutes before a shot, the gate valve that connects the MRS vacuum chamber to the NIF target-chamber vacuum is opened. After a shot, the CR-39 detector array is removed from the diagnostic for processing and analysis. Sections III A–III F describe the MRS components in detail.

### A. MRS configurations on OMEGA and the NIF

A summary of the MRS parameters and estimated errors is given in Table I. The efficiency and energy resolution (for 14 MeV neutrons) for each MRS configuration are shown at the bottom of the table. Each MRS parameter, and how it is characterized, is discussed in detail in Secs. IV A–IV D.

### B. Foil holder and blast shield

On both the OMEGA MRS and NIF MRS, the foil is protected by a blast shield (Figure 4). For the OMEGA MRS, a 500 $\mu$m thick stainless steel plate, positioned directly in front of the foil, is used as a blast shield. For the NIF MRS, a 1.57 mm thick (on average) tantalum plate positioned 5 mm in front of the foil is used as a blast shield. To withstand the impulse loading and debris from the NIF hohlraum, the thickness of the arm and blast shield was tapered to improve the robustness.

The MCNP neutron transport code[17] was used to determine the level of scattered neutrons from these blast shields and their impact on the MRS primary and DSn measurements. In these calculations, 14 MeV neutrons were emitted from the target chamber center (TCC) and transported through the MRS foil-holder arrangements. The results from those calculations are shown in Figure 5(a). The total OMEGA MRS fluence, per produced neutron, is higher than the NIF MRS because the foil is closer to the implosions (10 cm at OMEGA compared to 26 cm at the NIF). The simulations shown in

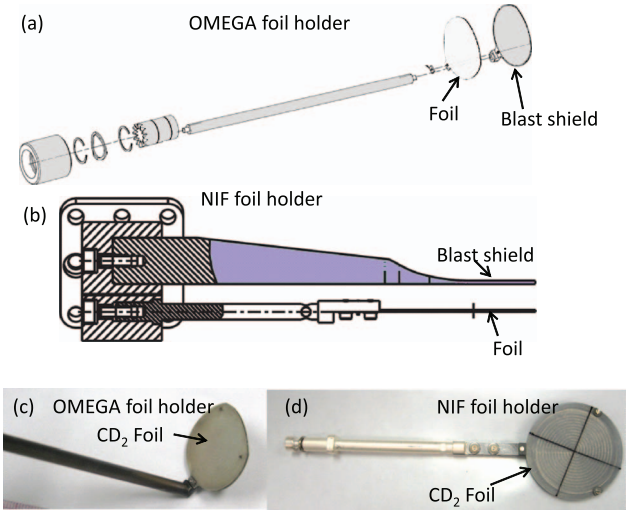


FIG. 4. (a) A CAD drawing of the OMEGA MRS foil holder, illustrating the 500 $\mu$m stainless steel blast shield, the foil, which is flush against the blast shield, and the insertion rod that attaches to the NDI. (b) A CAD drawing of the NIF MRS foil holder, which illustrates the tapered arm and Ta blast shield (described in the text), the foil holder attached directly to the foil and offset from the blast shield by 5 mm, and the bracket that attaches to the DIM. (c) OMEGA MRS foil holder with the 13.2 $cm^2$ low resolution $CD_2$ foil attached. (d) NIF MRS foil holder with the 12.8 $cm^2$ low-resolution $CD_2$ foil attached (blast shield not shown).

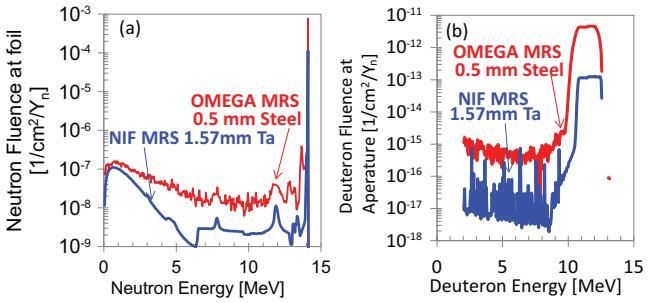


FIG. 5. (a) MCNPX simulated fluence of 14 MeV neutrons coming directly from the implosion and neutrons scattered by the foil blast shield for the OMEGA MRS (red curve) and the NIF MRS (blue curve). The OMEGA MRS foil blast-shield is 500 $\mu$m thick and made of stainless steel and the NIF MRS foil blast-shield is 1.57 mm thick (on average) and made of tantalum. The total NIF MRS neutron fluence, per produced neutron, is lower than the OMEGA MRS because the foil is further away from the implosion. (b) MCNPX simulated fluence of recoil deuterons at the magnet aperture that originate from the neutron-fluence spectra shown in (a). A 260 $\mu$m thick $CD_2$ foil (low resolution) was used in these simulations. As described in the text, the fluence of these recoil deuterons is insignificant when diagnosing high-$\rho$R implosions at OMEGA and the NIF.

Figure 5(a) are angle-integrated values. To assess the effect of the blast shield on the MRS DSn measurement, both the energy and angle of the scattered neutron, and the differential cross section for the elastic n-d scattering must be considered. The MCNPX[18] code was used to determine this and the results are shown in Figure 5(b), which give the recoil deuteron fluence at the MRS aperture. These calculations indicate that the blast shield adds an effective $\rho$R of 1.7 mg/cm$^2$ and 3 mg/cm$^2$ to the observed $\rho$R in a DT implosion at OMEGA and the NIF, respectively. Note that a 260 $\mu$m $CD_2$ foil alone also adds about 0.7 mg/cm$^2$ of $\rho$R from internal scattering. These numbers are $<$1% of typical cryogenic $\rho$R (at each facility), but are important for very low $\rho$R implosions. From these calculations, it was also concluded that the blast shield attenuates the inferred primary yield by $\sim$1% and 3.6%, at OMEGA and NIF, respectively, an important effect that must be considered.

### C. Magnet and its properties

The magnets for the OMEGA MRS and NIF MRS are nominally identical wedge-shaped, rare-earth (neodymium-iron-boron) permanent magnets (see Figure 6) manufactured by Dexter Magnetic Technologies, Inc.[19] Permanent magnets were selected, as they have several advantages over electromagnets. They can be much smaller and do not require a power supply or cooling systems. They do not suffer from startup/hysteresis concerns. Some disadvantages include relatively expensive raw material and they cannot be adjusted or turned off when not in use. The strength of the magnetic (B) field in permanent magnets depends slightly on the ambient temperature (described here in Kelvins [K]), which for these materials scales as $-0.11\%$ ($\delta$B/B)/K.[20]

The entrance and exit pole faces of the magnet are angled with respect to the incoming particle trajectories, creating a wedged-shaped field region. This focuses charged particles onto the detector plane, allowing the entrance aperture to

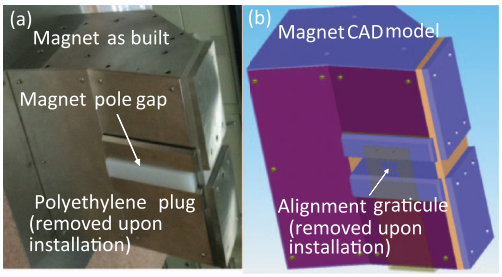


FIG. 6. (a) Image of the NIF MRS magnet built by Dexter Magnetic Technologies, Inc. The magnet pole gap has been plugged with polyethylene to prevent ferromagnetic objects from entering the $\sim$0.9 T field and possibly damaging equipment or causing injury (the plug was removed upon installation). (b) A CAD model of the MRS magnet with an image of the alignment graticules used to position and orient the magnetic field with respect to foil and CR-39 detectors. The magnets for the OMEGA MRS and NIF MRS are nominally identical but have slightly different, as built, field strengths.

be significantly larger for the same energy resolution.[3] This is an essential feature that for a fixed energy resolution dramatically increases the detection efficiency ($>$10 times) over simple bending-magnet designs. The magnet pole-gap is 3 cm across but the magnet aperture in front of the magnet decreases the acceptance opening to 2 cm in the direction perpendicular to the bending plane. The angled entrance-pole face relative to the direction of the incoming recoil particles produces a weak quadrupole moment that focuses particles in the transverse (non-dispersion) direction, helping to deflect particles away from poles (scattering of the poles would have a detrimental effect on the DSn measurement).[3]

The standard magnet aperture is 11 $\times$ 2 cm$^2$ and 10 $\times$ 2 cm$^2$ for the OMEGA MRS and the NIF MRS, respectively. Other apertures are occasionally used for special experiments. This often involves measurements of charged particles coming directly from the implosion (when the foil is not fielded). In the case of the NIF MRS, very small apertures will be used for diagnosing very high-yield implosions.

A finite element model of the magnetic field, developed by Dexter, is shown in Figure 7. The wedge shaped magnetic field peaks at $\sim$0.9 T in the symmetry plane of the magnet.

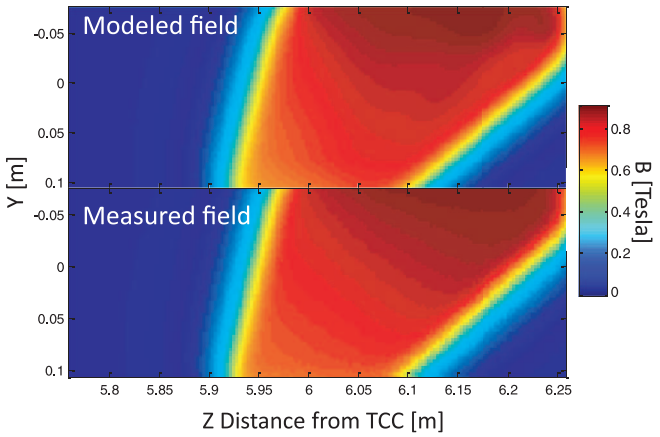


FIG. 7. Modeled and measured magnetic-field maps of the main B-field component for the NIF MRS (which is nominally identical to the OMEGA MRS magnet except for a slight difference in field strength, see Figure 8). A comparison of the images shows a very similar overall shape and maximum field strength. The magnet modeling and field measurements were performed by Dexter Magnetic Technologies Inc.

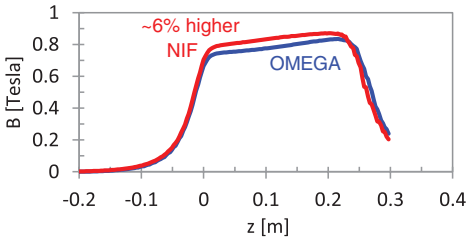


FIG. 8. A comparison of the OMEGA MRS and NIF MRS measured magnetic field strength. This line-out was taken through the center of the MRS line-of-sight. Z = 0 cm corresponds to the location of the magnet aperture at the pole entrance side, which is at 2.25 m from TCC at OMEGA and 5.96 m from TCC at the NIF (Z = 0 is also the location of the graticule in Figure 6).

The figure also shows the measured field map of the NIF MRS magnet. A comparison of the two field maps shows that the measured magnetic field is in good agreement with the modeled one.

A quantitative comparison between the measured OMEGA MRS and NIF MRS fields show that the as-built NIF MRS magnetic field is stronger by ∼6% than the OMEGA MRS magnetic field (see Figure 8). Despite this difference, both magnets perform very well (the differences are accounted for in the *in situ* calibration and modeling of the MRS).

### D. CR-39 detector array

An array of CR-39 detectors, positioned at the focal plane of the MRS, is used to detect the recoil particles produced in the conversion foil. CR-39 is a clear optical-quality plastic with a density of 1.3 g/cm$^3$ and molecular formula $C_{12}H_{18}O_7$ (all CR-39 detectors used by the MRS are TASTRAK manufactured by TASL Ltd).[21]

Signal particles, such as protons or deuterons, create trails of molecular damage as they travel through the CR-39 plastic. These trails of damage are revealed through an 80 °C, 6N NaOH "track etch," in which the damaged trails etch faster than the bulk material. The location, size, eccentricity, and contrast of the formed tracks on the CR-39 detectors are recorded using a digital microscope.[4,22] In some low signal-to-background (S/B) scenarios (S/B ≪ 1), the coincidence counting technique (CCT) can be applied using a series of staged track and bulk etches to dramatically reduce the background (often by two orders of magnitude), as described in detail in Ref. 23 (note that for the bulk etch used in CCT processing a mixture solution of NaOH/ethanol is also used). A histogram of track positions along the whole MRS detector plane is generated from the CR-39 track data. Future spectrometer designs are currently being considered to use advanced time-resolved detector systems, such as recoil ion streak-cameras for high neutron yield applications.[24]

As the CR-39 detectors in the array are accurately positioned and oriented with respect to the other components of the system (i.e., magnet, aperture, and foil), an energy spectrum of the recoil deuterons can be determined from the track-position histogram. Figure 9 shows the two CR-39 detector arrays for the OMEGA MRS and the NIF MRS. The base for the OMEGA MRS detector array is a cylindrical tube,

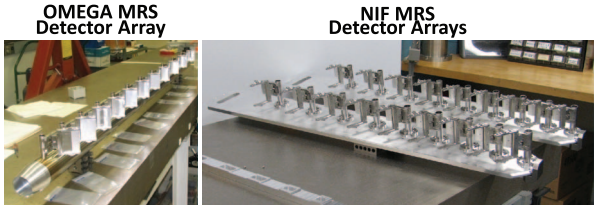


FIG. 9. Left: CR-39 detector array for the OMEGA MRS. The base for the OMEGA MRS detector array is a cylindrical tube with a nose cone, which latches onto an alignment pin inside the detector housing. Right: Two CR-39 detector arrays for the NIF MRS. The NIF MRS array is a flat "ironing board," which slides along a fin to a hard stop at the end of the array. Both systems use detector "flag poles," which position each CR-39 detector inside locking forks.

which slides upward into the detector housing where the nose cone attaches to an alignment pin. The alignment pin suffers from wear and tear during routine operations, and must be replaced regularly. This motivated a new design for the NIF-MRS detector array (sometimes called "ironing board"). The NIF-MRS detector array slides downward into the detector housing on a fin, and its location relative to the other system components is defined by a flat stainless-steel hard-stop at the low-energy end of the array. Images of the insertion procedure of the CR-39 detector arrays for the OMEGA MRS and NIF MRS are shown in Figure 10.

The CR-39 detectors are positioned at the focal plane of the MRS at which the recoil particles are at best magnetic focus (also best resolution). Each CR-39 detector is oriented in such way that the directions of the incoming recoil particles are nearly perpendicular to the detector surface, an important feature for optimal detection with CR-39 (also important for the coincidence counting technique).[23] The 11 OMEGA-MRS detector locations are illustrated in Figure 11. The NIF MRS detectors are located using the same guiding principles but due to different ion-optical properties of the system, only nine CR-39 detectors, spaced much closer, are used to cover about the same energy range.

The CR-39 detectors are held by forks that are attached to "flag poles." The forks also hold filters in front of the CR-39, which are used to range down incoming charged particles to energies for optimal CR-39 detection. Typically deuterons with energies approximately between 1 and 10 MeV and protons with energies between 1 and 8 MeV are readily detected with high S/B.[4] In low signal-to-background scenarios (S/B ≪ 1), the CCT is used, as mentioned earlier, which requires more careful filter considerations.[10,23]

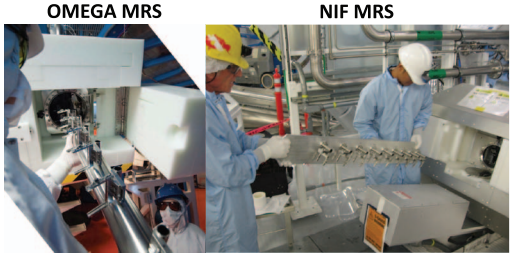


FIG. 10. The insertion of the CR-39 detector array into the OMEGA MRS (left) and NIF MRS (right). A door in the polyethylene shielding (described in detail in Sec. III E) allows access to the MRS vacuum chamber.

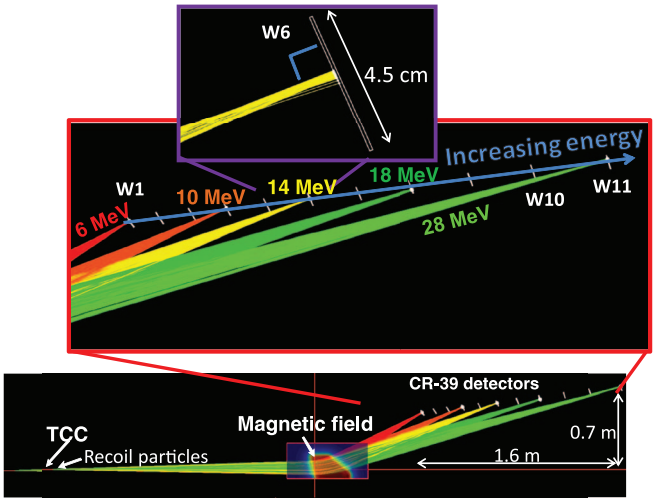


FIG. 11. Position and orientation of the 11 OMEGA MRS detectors (also called windows) along the focal plane. Each CR-39 detector is designated with a sequentially increasing (with energy) window number (W1, W2, etc.), as illustrated by several examples. The trajectories of recoil particles with proton equivalent energies of 6, 10, 14, 18, and 28 MeV are also shown. Each CR-39 detector is oriented to make sure the directions of the incoming recoil particles are nearly perpendicular to the detector surface, an important feature for optimal detection with CR-39. The nine NIF MRS detectors are located and oriented in a similar way but are spaced closer together due to different ion-optical properties of the system.

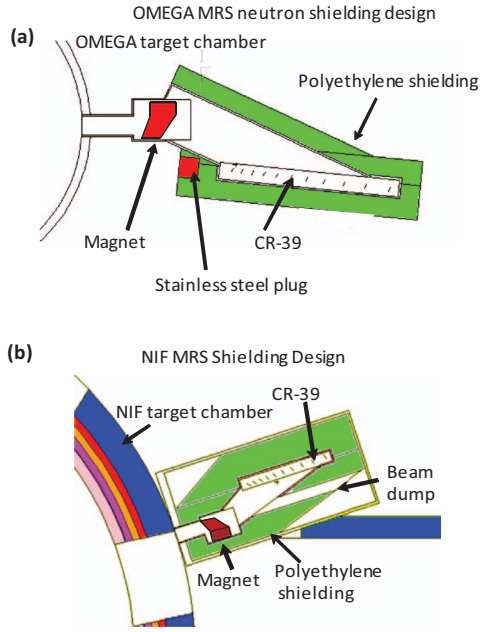


FIG. 12. (a) A schematic drawing of the OMEGA MRS neutron shielding design. A stainless steel plug is used to attenuate direct unscattered DT neutrons, while polyethylene around the MRS-detector housing is used to attenuate lower energy scattered neutrons. (b) A schematic drawing of the NIF MRS neutron shielding design. The NIF target chamber (10 cm of aluminum and 50 cm of concrete) significantly moderates and attenuates direct, unscattered 14 MeV neutrons, while the polyethylene around the whole diagnostic is used to moderate and attenuate lower-energy scattered neutrons.

The fork arrangement allows the CR-39 detector and appropriate filter in front to be inserted and locked into place. The position of the high-energy edge of the CR-39 detector is defined by two feet at the end of the fork. These are critical for the optimal position accuracy of the CR-39 detectors in the dispersive direction. Three dowel pins, two on the opposite side of the feet and one opposite the CR-39 label, are used to define the location of the CR-39 in the direction perpendicular to the dispersive direction. The CR-39 filters are made of thin strips of mylar, aluminum, or tantalum filter laid out along the active area of the detector. The filter increases in thickness with increasing energy of the recoil particles along the array. The NIF MRS CR-39 detector #7, which detects recoil deuterons from primary DT neutrons, uses an Al step filter with thicknesses ranging from 150 $\mu$m to 225 $\mu$m (maximum thickness with maximum energy on the window). For the lowest energy detectors (that require some minimal filtering to stop very low energy background ions) 3.5 $\mu$m mylar is used because it is more robust than Al or Ta, which are easily destroyed when the thickness is less than 10 $\mu$m. Also note that the (n,p) proton production cross section is about two times lower for Ta than for Al at 14 MeV,[25] making it an ideal filter when the neutron background at the MRS detector needs to be considered. However, Al is much less expensive than Ta and was, therefore, used when background considerations are relaxed, such as for measurements of the primary peak. Complete details about the OMEGA-MRS and NIF-MRS filter arrangements are discussed in Ref. 10.

### E. Neutron shielding

The background of primary neutrons and neutrons scattered by the chamber wall, diagnostics, and other structures around the MRS needs to be considered and reduced significantly. To suppress this neutron background, an extensive amount of shielding was installed around the MRS. Designing the shielding requires both a detailed understanding of the neutron background in the OMEGA and NIF target bays and careful consideration of the design and space requirements. Weight constraints also had to be considered. As CR-39 is insensitive to $\gamma$-rays and x-rays, it is the detector of choice for the MRS. Polyethylene was chosen as the shielding material. This material is highly hydrogenous, which makes it an effective moderator and attenuator of neutrons (especially at lower neutron energies). It should be pointed out though that high Z materials are more effective at higher neutron energies (>10 MeV) because inelastic processes provide greater moderation, on average, than elastic-scattering processes with hydrogen.[26] In the case of direct 14 MeV neutrons, it is advantageous to first use a high-Z material (such as iron or steel) to shield the detector from direct 14 MeV neutrons. A hydrogenous material is then used downstream to more effectively moderate and attenuate the lower-energy neutrons that passed through the steel. Figure 12(a) shows a schematic of the OMEGA MRS shielding design, which features a ~20 cm thick stainless steel plug that attenuates direct 14 MeV neutrons from the implosion and ~20 cm of polyethylene shielding placed around the detector housing that is used to shield scattered neutrons in the target bay. Figure 12(b) shows the NIF MRS shielding design. The 50 cm concrete (i.e., gunite) on top of the 10 cm thick aluminum target chamber attenuates direct 14 MeV neutrons, and 40 cm of polyethylene,

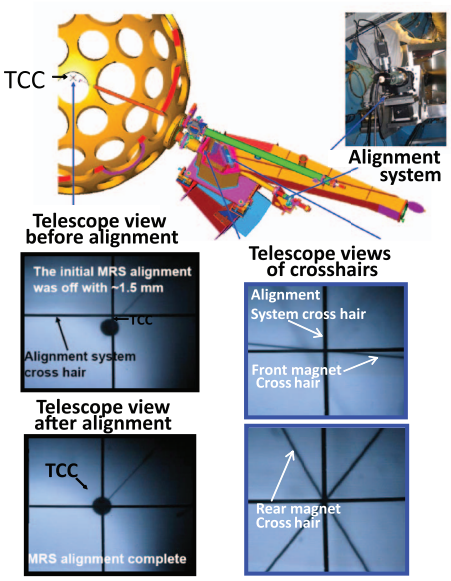


FIG. 13. Alignment procedure for the OMEGA MRS. Cross-hairs in the front and rear of the magnet, which define the MRS LOS, are aligned to the cross-hair in the alignment telescope that is behind the magnet. Using these cross-hairs, the MRS is pointed to TCC where a 1-mm backlit Au sphere is positioned (see the bottom left images). When the MRS is pointing towards TCC, the foil is inserted and centered on the MRS LOS at the specified distance from TCC. This alignment procedure is similar to the NIF MRS except for a minor difference, as described in the text.

surrounding the MRS, provides shielding from lower-energy scattered neutrons in the target bay (see Sec. VII).

### F. Alignment

The MRS system is aligned to TCC using a set of cross-hairs and a telescope system, as depicted in Figure 13 for the OMEGA MRS. Cross-hairs in the front and rear of the magnet define the MRS LOS. These cross-hairs are first aligned to another set of cross-hairs in the alignment telescope. Using the aligned magnet cross-hairs, the MRS is pointed towards TCC where a 1 mm backlit Au sphere is positioned. After the MRS is correctly aligned to TCC, the foil is inserted and centered on the MRS LOS at the specified distance from TCC. After the alignment process, the cross-hairs are removed and the magnet aperture is subsequently installed for shot operations. A similar procedure is used for the NIF MRS, except that a specially designed lighting system, which uses a scribed cross-hair on the foil and the cross-hairs of the alignment telescope, allows for the foil alignment to be verified before every shot.

## IV. CHARACTERIZATION OF THE MRS PARAMETERS

A summary of the spectrometer parameters and associated uncertainties are given in Table I. The characterization of each parameter listed in that table is discussed in detail in this section. In addition, as the $CD_2$ foil is not an off-the-shelf item that can be purchased, this section also describes how they are manufactured to the required tolerances.

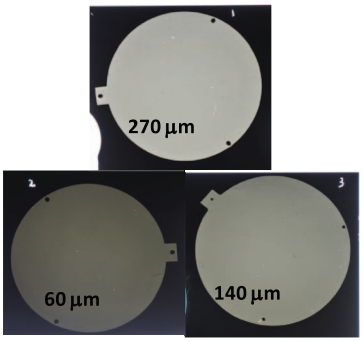


FIG. 14. X-ray radiographs of $CD_2$ foils made by GA. These images show that the $CD_2$ foils have excellent uniformity. The difference in apparent contrasts is due to higher X-ray attenuation by the thicker foils.

### A. Manufacturing $CD_2$ foil

The $CD_2$ foils are manufactured from a deuterium powder that is manufactured by ISOTEC Sigma Aldrich.[27] From this powder, which contains a deuterium purity of 98% (at. %), the first $CD_2$ foils for the OMEGA MRS were developed and produced by Fletcher *et al.* at SUNY Geneseo.[28] Two manufacturing methods were used: the xylene and heated-press methods. In the xylene method, the $CD_2$ powder is dissolved into a xylene liquid solvent under heat. When exposed to the heat for a certain period of time (minutes to hours), the solvent evaporates, leaving a thin foil of $CD_2$ at the bottom of the container. In the heated-press method, the powder is pressed in a mold under high pressures at an elevated temperature, resulting in a uniform foil.[28] Both types of foils have been used for the OMEGA MRS and produced good data. The $CD_2$ foils are now produced by General Atomics (GA),[29] who only used the heated-press method. From the experience gained at SUNY Geneseo, they improved the manufacturing process and are producing high quality foils. X-ray radiographs of the foils (see examples in Figure 14) show foils with excellent uniformity and that are free of voids, microstructure defects, and cracks.

### B. Characterization of the $CD_2$-foil density, area, and thickness

The average density of the $CD_2$ foil is determined from mass and volume measurements. The density of the first foils made was $1.03 \pm 0.03$ g/cm$^3$, which should be compared to the density of 1.08 g/cm$^3$ for pure deuterated polyethylene.[30] This difference is due to the introduction of microscopic voids during the preparation of these first foils. The average density of the newer (after 2010) foils is 1.07 g/cm$^3$ and much closer to the literature value due to the mitigation of void formation. The density variation of these foils is as low as $\pm 2\%$.

The solid angle subtended by the foil is determined from the foil area (A) and foil distance from the implosion (d),

$$\Omega_n = \frac{\mathrm{A}}{4\pi d^2}. \quad (5)$$

At OMEGA, the NDI is used to position the foil at a nominal distance of 10 cm from the implosion or TCC. As the foil holder tends to get warped over time (due to intense

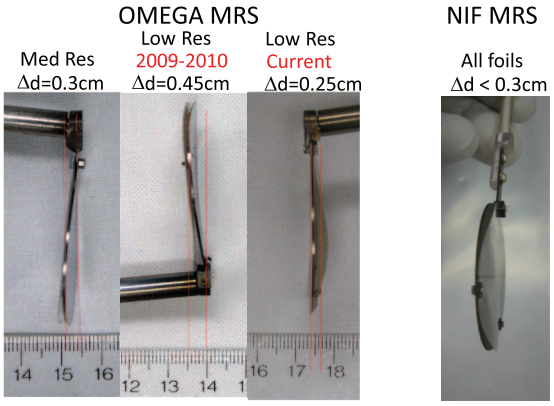


FIG. 15. Images of the $CD_2$ foils for the OMEGA MRS and NIF MRS, which illustrate the foil-holder warping and foil-cupping issues. The warping issue, which is mainly caused by intense heat exposure, only exists for the OMEGA MRS, as no protective blast shield is positioned in front of the foil holder (a 500 $\mu$m thick stainless steel plate in front of and in direct contact with the foil). The foil-cupping issue, on the other hand, exists for both the OMEGA MRS and NIF MRS. These issues result in a distance offset of about 2–5 mm from the nominal value for the OMEGA MRS and up to 3 mm for the NIF MRS. In case of the NIF MRS, this is a less significant issue as the nominal foil distance is 26 cm.

heat exposure), and the fact that the foil is often not attached flush to the holder (cupping), the actual distance of the foil to TCC is different from the nominal value (Figure 15), which must be accounted for in the determination of the detection efficiency (Eq. (3)). Due to the energy and impulse-loading constraints on the NIF, the foil for the NIF MRS is positioned at a distance of 26 cm from TCC (DIM 90°–315° is used for the positioning of the foil). The foil is also positioned behind a protective blast shield, which reduces the impact on the foil to a minimum. On the NIF, only cupping of the foil is a minor issue because the foil is positioned farther away from TCC than on OMEGA. Nevertheless, the foil holder is being redesigned with a new retaining ring to help mitigate this issue.

Two approaches have been used to determine the area of the $CD_2$ foil. In the first method, image analysis was used to determine the area from a photo taken of the foil. This method was only applied to the OMEGA MRS foils. In this analysis, a known area of reference, covering a certain number of pixels in the image, was used to convert the number of pixels of the foil into an area (see Figure 16(a)). Multiple measurements with different area references indicated an uncertainty of $\pm 0.3$ cm$^2$ associated with this method. Using this method, the low resolution foil for the OMEGA MRS was determined to be 13.2 cm$^2$ $\pm$ 0.3 cm$^2$. In the second method, the $CD_2$ foils were precision-die cut by GA, and the uncertainty associated with this method was also estimated to be $\pm 0.3$ cm$^2$. This method was applied to all NIF-MRS foils.

The average thickness of the low-resolution OMEGA foil was measured with a micrometer to be 261 $\mu$m with a standard deviation of 18 $\mu$m (thickness map is shown Figure 16(b)). The uncertainty in the average thickness is $\pm 2$ $\mu$m from the systematic uncertainty of the micrometer. The NIF MRS foils were measured at GA using a similar method with an absolute uncertainty of $\pm 2$ $\mu$m, see Figure 17(b). The standard deviation of the low resolution NIF MRS foil thickness is 5 $\mu$m. The high-mode surface roughness of the foil was evaluated for a large sample of foils using an interferometry method. It was found that the roughness was on average $\sim 0.2$ $\mu$m RMS for these foils.

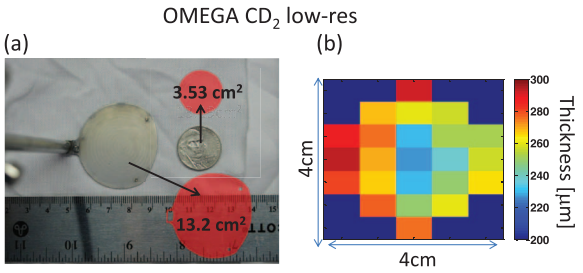


FIG. 16. Image of the OMEGA MRS low resolution $CD_2$ foil. The measured area of the foil is 13.2 $\pm$ 0.3 cm$^2$. To avoid interference between the foil and gate valve during the foil insertion process, the shape of the foil had to be noncircular (this is only an issue for the foils larger than 11 cm$^2$). Also shown, is a United States nickel used as a reference area for the foil area measurement, as described in the text. (b) The measured thickness profile of the OMEGA low-resolution foil. The mean thickness is 261 $\pm$ 2 $\mu$m, and the thickness variation across the foil is characterized by a standard deviation of 18 $\mu$m.

### C. The differential cross section for elastic n-d scattering in the laboratory system

The differential cross section for the elastic n-d scattering in the laboratory system for neutron energies in the range 3.5–18 MeV is an important parameter for determining the detection efficiency for the MRS (see Eq. (3)). The uncertainty in the evaluated cross sections, obtained from the ENDF/B-VII.0 nuclear database,[31] plays an important role when determining the absolute spectrum from the measured recoil-deuteron spectrum. As these cross sections are well known for the neutron energies of relevance, the MRS detection efficiency (and therefore the absolute neutron spectrum) can be determined with high accuracy. Figure 18(a) shows the angular differential cross sections in the laboratory system for neutron energies of 5.6 and 14.17 MeV. Figure 18(b) shows the total cross section for the n-d elastic scattering as a function of neutron energy. The geometric consideration of the foil and magnet aperture of the cross section is made using the Monte Carlo code MCNPX.[32] The uncertainty in the forward scatter differential cross section at 14 MeV is 2.3%.[33] For several commission experiments, a $CH_2$ foil was used to produce recoil protons. In these cases, the n-p elastic scattering was used, also

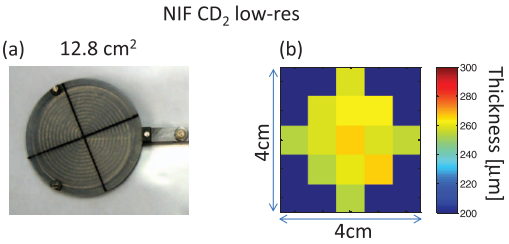


FIG. 17. Image of the NIF MRS low resolution $CD_2$ foil (produced and characterized by GA). The area and average thickness of this foil is 12.8 $\pm$ 0.3 cm$^2$ and 259 $\pm$ 2 $\mu$m, respectively. The thickness variation across the foil is characterized by a standard deviation of 5 $\mu$m. Note that the blue areas are outside the foil.

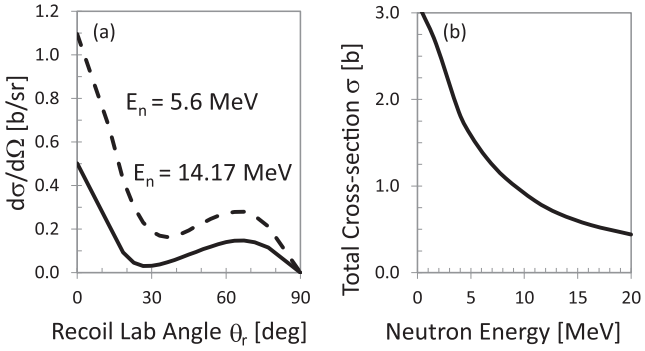


FIG. 18. (a) The differential cross section for the elastic n-d scattering at neutron energies of 5.6 (dashed line) and 14.17 MeV (solid line) as a function of laboratory scattering angle. The laboratory scattering angle $\theta_r$ is the angle between the incoming neutron and the outgoing recoil deuteron. These cross sections were obtained from the ENDF/B-VII.0 library.[31] The location and geometry of the aperture with respect to the foil is such that only forward scattered recoil particles ($\theta_r \sim 0$) are accepted. (b) The total cross section for the elastic n-d scattering, which can be obtained by integrating the angular differential scattering cross sections, shown in (a). The total cross sections were also obtained from the ENDF/B-VII.0 library.[31]

obtained from the ENDF/B-VII.0,[31] which is nearly isotropic in the center-of-mass frame at 14 MeV in contrast to n-d.

### D. The magnet aperture

For the OMEGA MRS and the NIF MRS, the magnet aperture is an 11 × 2 cm$^2$ and 10 × 2 cm$^2$ rectangular hole, respectively; cut out of a 500 $\mu$m thick tantalum plate. Highly accurate electrical discharge machining (EDM) was used to manufacture these apertures. The estimated uncertainty in the aperture area is ±0.2 cm$^2$.[5] As the aperture is directly attached to the wedge shaped magnet (Figure 19), it is tilted with 14.2° with respect to the incoming recoil protons or deuterons (as discussed in Sec. III). This reduces the effective aperture area with 3%. As the distance of the aperture relative to the $CD_2$ foil is 215 cm and 570 cm on the OMEGA MRS and NIF MRS, respectively, the positioning error in the location of the aperture along the MRS LOS has an insignificant impact on the detection efficiency.

It was recently found on OMEGA that the MRS-foil inserter, NDI, interferes slightly with the path of the recoil-deuteron beam, defined by the foil area and magnet aperture. The geometry is illustrated in Figure 20. As a consequence, a

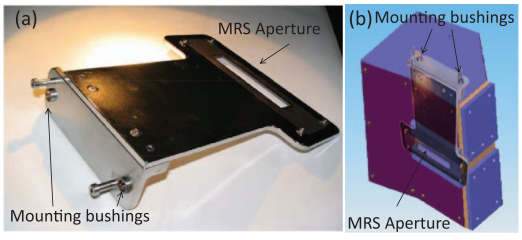


FIG. 19. (a) Image of the OMEGA MRS 11 × 2 cm$^2$ aperture attached to the mounting plate, which attaches to the front of the magnet. (b) Image of MRS aperture super-imposed on a CAD drawing of the MRS magnet to illustrate the relative location of the aperture on the magnet and where the aperture plate attaches.

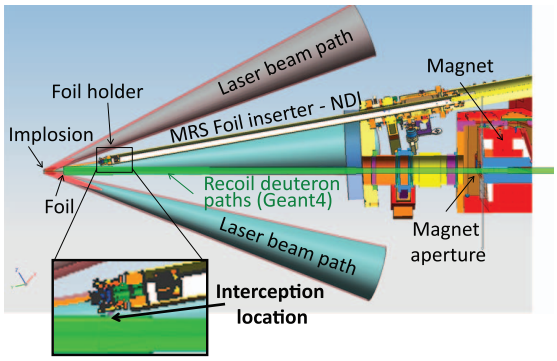


FIG. 20. Illustration of the OMEGA MRS and the MRS foil inserter (NDI) with super-imposed deuteron trajectories simulated with Geant4. The location where the NDI intercepts the path of the recoil deuterons from the foil is close to the coupling between the foil-holder arm and the NDI.

fraction of the recoil deuterons do not reach the aperture. This interception produces an asymmetric signal distribution in the direction perpendicular to the dispersion plane. Data obtained with the OMEGA MRS operated in medium and low resolutions illustrate this asymmetric behavior, as shown in Figure 21. These data were obtained when diagnosing DT-gas filled CH-capsule implosions. The black dashed curves in the figures are simulated signal distributions when the NDI does not intercept the recoil-deuteron beam, and the blue dashed curves, which give the best fits to the data, are simulated signal distributions when the NDI intercepts the recoil-deuteron-beam path as shown in Figure 20. The best fits to the data indicate that a correction factor of 0.86 ± 0.013 should be applied to the MRS-detection efficiency for the low-resolution foil (uniformly over all energies) and 0.87 ± 0.013 for the medium-resolution foil. Engineering solutions to this issue

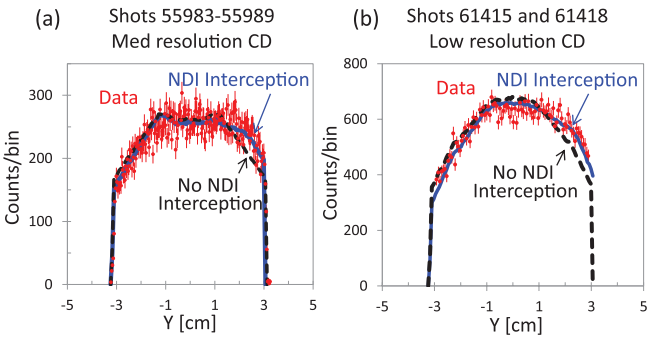


FIG. 21. (a) Measured and simulated signal distributions in the direction perpendicular to the bending plane (geometry illustrated in Figure 20) for the OMEGA MRS operated in medium resolution. The data was summed over shots 55 983–55 989. The dashed black curve represents a simulation where the NDI does not intercept the recoil-deuteron beam and the solid blue curve represents a simulation with the NDI intercepting the recoil-deuteron beam. Both simulations are normalized to the measure data. The simulation of the NDI interception was obtained by adjusting the height of NDI foil-holder coupling until the best fit to the data was found (a ~2–3 mm incursion into the MRS LOS). (b) Same modeling as in (a), but for the MRS operated in low resolution compared to data obtained from a summation shots 61 415 and 61 418. Both cases indicate a detection-efficiency reduction of 13%–14% due to the NDI interception for all deuteron energies. An engineering solution to this issue is currently being implemented. This interception issue is not present at the NIF.

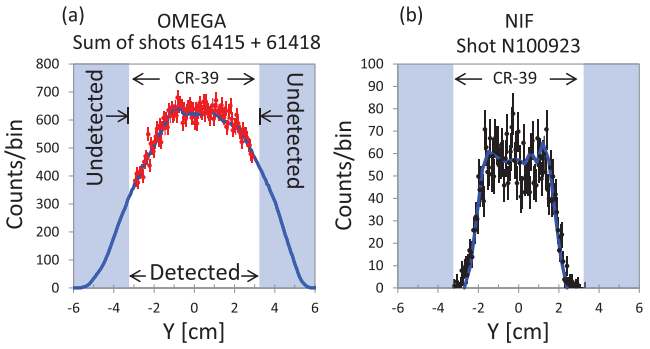


FIG. 22. (a) Measured and simulated primary signal distributions in the direction perpendicular to the bending plane for the OMEGA MRS operated in low resolution, which indicate a transmission of $T(12.5) = 0.79 \pm 0.03$ at a deuteron energy of 12.5 MeV (which corresponds to a neutron energy of about 14 MeV). (b) Measured and simulated primary signal distributions in the direction perpendicular to the bending plane for the NIF MRS operated in low resolution, indicating a transmission of 100% at this energy (this is true for all energies).

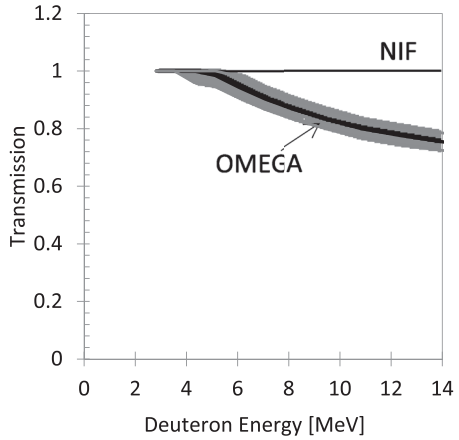


FIG. 23. Transmission as a function of deuteron energy for the OMEGA MRS (solid line) and NIF MRS (dashed line). The uncertainty in the OMEGA MRS transmission function, inferred from experiments with different aperture sizes, is shown by the grey region around the solid line. Due to the ion-optical properties of the NIF MRS, the transmission is 1.0 for all deuteron energies.

are currently being implemented. This interception issue is not present at the NIF, as a totally different foil insertion mechanism is used.

All deuterons that enter the aperture are not detected with the OMEGA MRS as their spatial spread in the direction perpendicular to the bending plane is larger than the length of the CR-39 detectors. As a result, a fraction of the deuterons selected by the aperture will not be recorded by the CR-39 detector array by design (also discussed in Sec. III). This is accounted for in the detection-efficiency calculation, through the transmission parameter $T(E_d)$. $T(E_d)$ decreases with increasing deuteron energy because the deuteron-beam path diverges in the direction perpendicular to the bending plane and the CR-39 detectors covering higher energies are further away from the magnet, resulting in a distribution at the detector that is wider. To illustrate this effect, a simulated primary signal distribution (perpendicular to the dispersion direction) using the OMEGA MRS operated in low-resolution mode is shown and compared to data in Figure 22(a). The simulation indicates that $T(12.5) = 0.79 \pm 0.013$ (averaged over the primary peak), resulting in 21% loss of the recoil deuterons. For comparison, simulated and experimental NIF-MRS data are shown Figure 22(b), which illustrates that T = 1.0 (this applies to all energies). This is due to better ion-optical properties of the system. A plot of the transmission as a function of deuteron energy for OMEGA MRS and the NIF MRS is shown in Figure 23.

## V. *AB INITIO* AND *IN SITU* ENERGY CALIBRATION

Through the MRS response function, the location of each recorded track on the CR-39 detectors can be related to the energy of the recoil particle and energy of the neutron that produced the recoil particle. The MRS response is modeled using the Monte Carlo code Geant4,[6] a C++ based particle transport toolkit commonly used in the particle physics community. Its generality and powerful feature-base has made it a very useful tool for this application.

### A. *Ab initio* energy calibration using Geant4

Several Geant4 models of the MRS have been developed for a variety of configurations. An illustration of one such model is shown in Figure 24. In this model, neutrons are transported to the foil from a point source positioned at TCC. At the foil, a small fraction of the neutrons produce recoil protons or deuterons, some of which are forward scattered and selected by the aperture in front of the magnet. The selected recoil particles are transported through the 3D magnetic field map. As the magnet is a focusing device in the dispersive plane, the particle trajectories for a specific energy are focused to a point at the focal plane of the spectrometer where the CR-39 detectors are positioned. When the recoil particles hit the CR-39 detectors, their energy and location are recorded and stored as well as the neutron energy.

Examples of *ab initio* modeled response functions for OMEGA MRS operated in high, medium, and low-resolution $CD_2$-foil configurations, discussed in Table I, are illustrated in Figure 25(b). These recoil-deuteron spectra were calculated using the primary DT neutron spectrum shown in Figure 25(a) ($Y_n = 3 \times 10^{13}$, $T_i = 5$ keV).

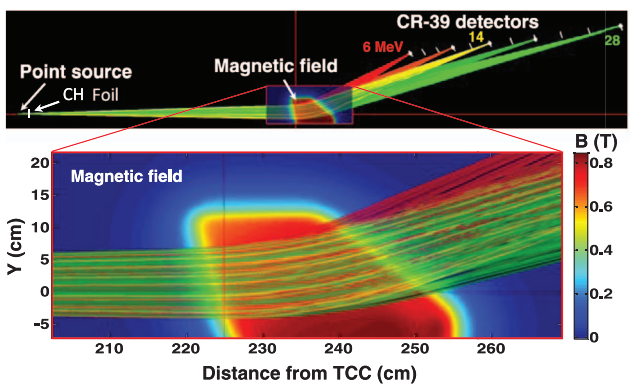


FIG. 24. An illustration of a Geant4 response model of the OMEGA MRS, featuring a simulation of 6, 10, 14, 18, and 28 MeV protons.

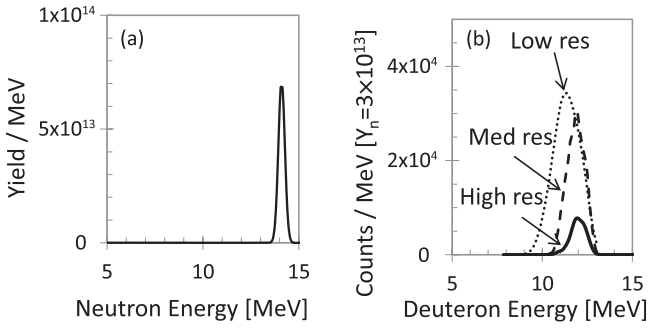


FIG. 25. Examples of *ab initio* modeled response functions for the OMEGA MRS. (a) Primary DT neutron spectrum ($Y_n = 3 \times 10^{13}$, $T_i = 5$ keV) used in these calculations. (b) Recoil-deuteron spectra calculated for the $CD_2$ high, medium, and low-resolution configurations (see Table I). As shown by these spectra, there is a tradeoff between efficiency and energy resolution.

*Ab initio* modeling of the NIF MRS response was conducted for different configurations prior to installation. Figure 26 shows the response for the MRS operated in high, medium, and low-resolution mode (see Table I). The DT neutron spectrum ($Y_n = 10^{14}$, $T_i = 5$ keV) used in these calculations is illustrated in Figure 26(a).

### B. *In situ* energy calibration experiments of the as-built systems

A series of *in situ* energy-calibration experiments were conducted to check the performance of the as-built OMEGA MRS[8] and the NIF MRS. As the *ab initio* modeling used nominal spectrometer settings, this type of calibration experiment is required to quantify a possible misalignment of the magnet, detectors, and small changes in the magnetic field unaccounted for in the modeling. For these experiments at OMEGA, a series of DT-gas filled CH capsules with a nominal diameter of 850 $\mu$m, a fill pressure of 15 atm, and shell thicknesses of 15 $\mu$m were imploded with a 1 ns square laser pulse shape, delivering ~23 kJ of UV-energy. Primary neutron yields in the range of $\sim 10^{13}$ to $\sim 3 \times 10^{13}$ and $T_i$ in the range of 5–6 keV were used to obtain an accurate energy calibration of the MRS. The Doppler broadened primary DT neutrons were used to produce recoil protons and deuterons from a 100 $\mu$m $CH_2$ foil and 60 $\mu$m $CD_2$ foil, respectively. This provided two well-known calibration points at a proton energy of 13.9 MeV and a deuteron energy of 12.4 MeV. The deuteron energy corresponds to a proton equivalent of 24.6 MeV (this number is determined by the mass ratio times the deuteron energy with a small relativistic correction). These experiments were repeated with different thicknesses of tantalum foil positioned behind the $CH_2$ and $CD_2$ foils to obtain calibration points at various recoil-particle energies.[8] The results from those experiments are shown in Figure 27(a), in which the proton equivalent energy at the center of a CR-39 detector is plotted as a function of detector-window number (illustrated in Figure 11). Figure 27(b) shows the determined calibration error using the nominal *ab initio* simulated energy calibration (dashed curved) and the *in situ* energy calibration (solid curve). A −1.1% uniformly scaled magnetic field provided an improved description of the data over the entire detector array, improving the proton equivalent energy error from a systematically shifted 430 keV to a symmetric ±160 keV (root-mean-square of error). This translates to a neutron energy error of ±100 keV when using the $CD_2$ foil.

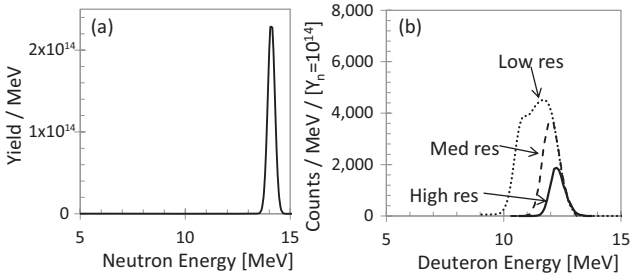


FIG. 26. Examples of *ab initio* modeled NIF MRS-response functions. (a) Primary DT neutron spectrum ($Y_n = 10^{14}$, $T_i = 5$ keV) used in these calculations. (b) Recoil-deuteron spectra calculated for the high, medium, and low-resolution $CD_2$-foil configurations (see Table I). As shown by these spectra, there is a tradeoff between efficiency and energy resolution for the NIF MRS.

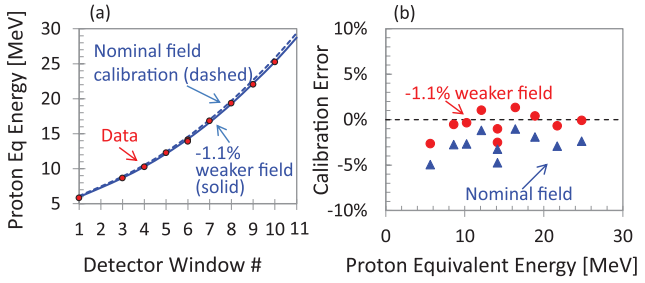


FIG. 27. (a) Measured and modeled energy (proton equivalent) as a function of detector window for the OMEGA MRS. The dashed curve was determined from the *ab initio* modeling of the MRS, in which a nominal magnetic field was used. The solid curve represents the *in situ* energy calibration of the MRS, in which the strength of the magnetic field was reduced by 1.1%. The data were obtained using the primary DT neutron spectrum and $CH_2$ and $CD_2$ foils. The energies below 15 MeV were probed by recoil protons from a $CH_2$ foil, while energies above 15 MeV were probed with recoil deuterons from a $CD_2$ foil. (b) Estimated calibration error calculated from the difference between the particle energy and the energy inferred from the calibration for the nominal field (blue triangles) and the −1.1% weaker field (red circles). The estimated energy error is improved from 430 keV to a symmetric ±160 keV (proton equivalent energy) when applying the −1.1% field correction.

*In situ* energy calibration data were obtained similarly with the NIF MRS[9] when operated with a medium resolution $CD_2$ foil (Table I). In these experiments, the primary DT neutron spectrum from a DT gas-filled $SiO_2$ capsule implosion (shot N101212) and a cryogenic DT capsule implosion (N110914) was used. For the N101212 shot, a 75 $\mu$m thick Ta filter, behind the foil, was used to reduce the average recoil-deuteron energy from 12.0 MeV to 8.4 MeV (23.8 MeV and 16.7 MeV proton equivalent energies). This provided two well-known calibration points. A third experiment (N110722) using $D^3He$ protons from a $D^3He$ gas-filled exploding-pusher implosion provided another calibration point. In this experiment, a 196 $\mu$m stainless steel (SST-410) "split-filter" with a rectangular hole in it replaced the $CD_2$ to obtain two proton-energy calibration points at ~14.7 MeV and ~11.2 MeV. The split-filter configuration allows the proton energy incident on the foil to be measured through the hole, while

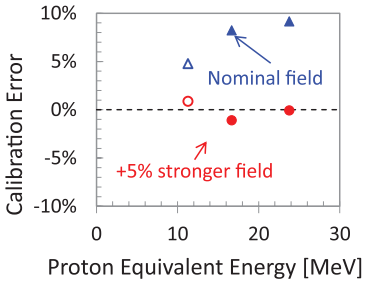


FIG. 28. Calibration error of the NIF MRS when using the nominal field (blue triangles) and the +5% stronger field (red points). The solid points were determined using $CD_2$ foil produced deuterons, while the open points were determined using $D^3He$ protons. Note the $D^3He$ split-filter configuration produces only one calibration point as the exact $D^3He$ proton energy must be determined using the unfiltered region because of electric field acceleration[34] and energy-loss uncertainty (and possible asymmetry). The estimated energy error improved from a shifted 1.6 MeV (proton equivalent energy) to ±120 keV using the +5% field correction, which corresponds to an error of ±70 keV neutron energy when using the $CD_2$ foil.

providing a lower energy calibration point through the filter. As the birth spectrum is not totally known due to energy-loss effects and possibly energy upshifts due to electric fields around the capsule,[34] compact Wedge-Range-Filter (WRF) spectrometers were also used to measure the emitted proton spectrum.[4] Using these data, the error in the NIF MRS *ab initio* calibration with the nominal field was determined (Figure 28). When the field strength is increased by 5%, an excellent match to the experimental observations is observed, resulting in an energy-calibration error of ±120 keV proton equivalent energy, which corresponds to ±70 keV neutron energy when using the $CD_2$ foil.

## VI. GEANT4 SIMULATIONS OF THE MRS-RESPONSE FUNCTION

With an understanding of the as-built MRS on OMEGA and the NIF, a complete MRS response function for the different configurations was generated with Geant4. This is accomplished by computing the deuteron spectrum at the CR-39 detector array for neutron energies of 3–27 MeV in steps of 100 keV. The output of this calculation is a 240 × 240 response matrix. This matrix allows a modeled neutron spectrum to be directly folded with the MRS-response function in a simple step, instead of running a full Geant4 simulation each time a measured MRS spectrum is analyzed. As each MRS configuration has a foil with different measured thickness and area, it must have its own specific response matrix. The OMEGA-MRS-response matrices for the high-resolution (5.7 $cm^2$ area 62 $\mu$m thick), medium-resolution (10.64 $cm^2$ area 164 $\mu$m thick), and low-resolution (13.19 $cm^2$ area 261 $\mu$m thick) $CD_2$ foils are shown in Figure 29.

Figure 30(a) illustrates MRS spectra summed over a series of 20 $\mu$m CH-capsule OMEGA implosions (shots 54 472–54 474) and 15 $\mu$m CH-capsule OMEGA implosions (shots 58 165, 58 209, 58 210, and 54 465–54471), which produced 3.2 × $10^{13}$, 5.0 × $10^{13}$, and 5.0 × $10^{14}$ primary neutrons, respectively (these yields were measured with the nTOF diagnostic).[35] The green spectrum was measured while

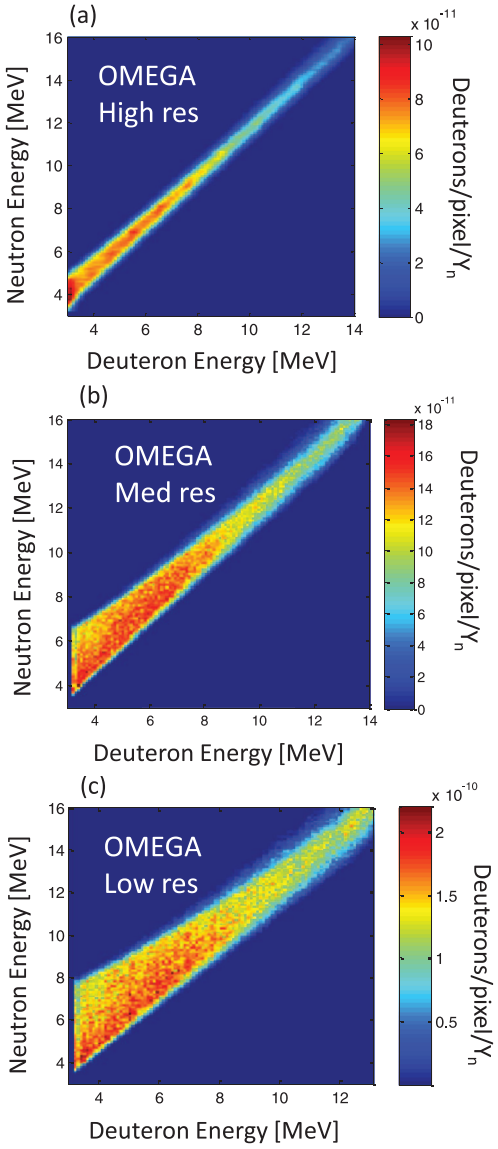


FIG. 29. The response matrices for the OMEGA MRS operated in high (a), medium (b), and low resolution (c) (see Table I for these spectrometer configurations). As shown by these matrices, the energy broadening is more significant at lower energies. The response matrix is used to determine the neutron spectrum from the measured recoil deuteron spectrum. This is done by folding a modeled neutron spectrum with the response matrix and adjusting it until best fit to the measured spectrum is found.

the MRS was operated in high resolution mode, the blue in medium resolution, and the red spectrum in low resolution. The modeled neutron spectra that provide the best fit to the measured spectra are shown in Figure 31(b) using a forward-fit technique.[5,10] Also, the total neutron yield determined from the measured spectra is in agreement with the nTOF yields (discussed in Ref. 36).

The response matrices for the NIF MRS operated with a low-resolution (12.78 $cm^2$ area and 259 $\mu$m thick), a medium resolution (12.8 $cm^2$ area and 138 $\mu$m thick), and a high-resolution $CD_2$ foil (12.8 $cm^2$ area and 47 $\mu$m thick) are shown in Figure 31.

Primary spectra obtained with the NIF MRS operated in different configurations are shown in Figure 32. These

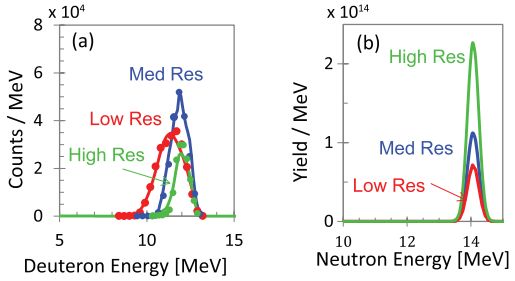


FIG. 30. (a) OMEGA MRS spectra summed over a series of 15 $\mu$m CH-shell capsule implosions (blue and green spectra) and 20 $\mu$m CH-capsule implosions (red spectrum). Integrated implosions 54 465–54 471 (green), 58 165 and 58 209–58 210 (blue), and 54 472–54 474 (red) produced 1.0 × $10^{14}$, 5.0 × $10^{13}$, and 3.2 × $10^{13}$ primary neutrons, respectively. Due to different energy losses in the $CD_2$ foils, the average energy of the deuterons is 12.0, 11.8, and 11.4 MeV for the high, medium, and low resolution foils, respectively. Note that kinematics also dictate some energy down-shift of the recoil deuterons. (b) Modeled neutron spectra that provide the best fits to the measured recoil-deuteron spectra in (a).

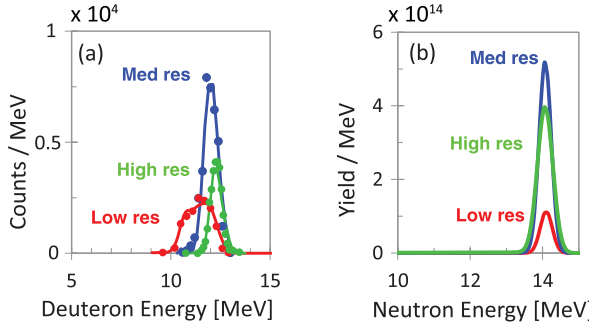


FIG. 32. NIF MRS spectra obtained from three 4 $\mu$m $SiO_2$-capsule implosions (N100923, N1001030, and N110217, which produced 4.8 × $10^{13}$, 2.3 × $10^{14}$, and 2.0 × $10^{14}$ neutrons, respectively). The green, blue, and red spectra were obtained when the MRS was operated in high-resolution, medium-resolution, and low-resolution mode, respectively. Due to different energy losses in the $CD_2$ foil, the average energy of the deuterons is 11.4 MeV for low resolution, 12.0 MeV for medium resolution, and 12.3 MeV for high resolution. (b) Modeled neutron spectra that provide the best fits to the measured recoil-deuteron spectra in (a).

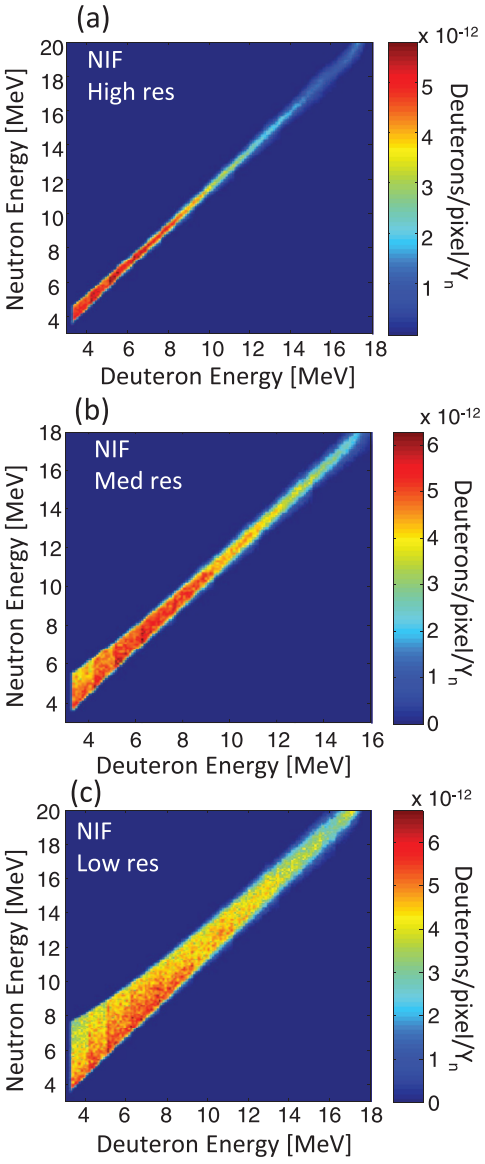


FIG. 31. Response matrices for the NIF MRS operated in high (a), medium (b), and low-resolution (c) modes.

spectra were obtained from three 4 $\mu$m thin-glass DT implosions (N100923, N1001030, and N110217), which produced yields of 4.8 × $10^{13}$, 2.3 × $10^{14}$, and 2.0 × $10^{14}$, respectively. The green, blue, and red spectra were obtained when the MRS was operated in high-resolution, medium-resolution, and low-resolution mode (see Table I), respectively. The modeled neutron spectra that provide the best fit to the measured spectra are shown in Figure 31(b). The total neutron yields determined from the measured spectra are in good agreement with activation yields (discussed in Ref. 36).

## VII. NEUTRON-BACKGROUND AND SHIELDING DESIGN SIMULATIONS

The choice of using CR-39 for the MRS detector was based in part on its insensitivity to x-rays, $\gamma$-rays, and EMP, and its 100% sensitivity to charged particles.[4] CR-39 is, however, somewhat sensitive to neutrons (>0.1 MeV).[4,25] The efficiency for detecting 14.1 MeV neutrons is 6 × $10^{-5}$ and $10^{-4}$ for 2.45 MeV neutrons,[25] which makes neutrons a source of background for low-signal applications such as down-scattered neutron measurements (CR-39 intrinsic noise[4,23] is another important background that must be considered in low-yield applications). It is, therefore, necessary to quantitatively model the neutron-background environment around the MRS and mitigate it by optimizing the shielding around the system (and use other means of mitigation such as CCT).[23] This section discusses the modeling of the neutron background and the optimal shielding design for both the OMEGA MRS and NIF MRS. For the OMEGA MRS, modeling of the neutron background, with and without shielding, was verified by measurements. The shielding built around the OMEGA MRS and the NIF MRS is shown in Figure 2.

### A. Neutron background characterization and shielding design for the OMEGA MRS

Neutrons interact with the CR-39 through nuclear elastic scattering, (n,p) reactions, (n,$\alpha$) reactions, and carbon

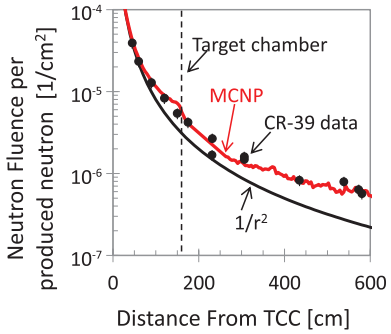


FIG. 33. Measured and simulated neutron fluence per produced neutron as a function of distance from the implosion (or TCC). Data and simulations are contrasted to the $1/4\pi R^2$ scaling (black curve), which illustrates the effect of scattered neutrons.

breakup. These processes generate charged particles, which leave trails of damage in the CR-39 that are revealed by the standard etching process, as described in detail in Ref. 25. The principal sources of background neutrons are direct primary neutrons and neutrons scattered by the chamber, target bay walls, diagnostics, and other structures surrounding the MRS. Although the CR-39 efficiency for detecting these neutrons is small, the MRS needs to be enclosed by polyethylene shielding to suppress the neutron background to the required level for measurements of DSn. To optimally design the shielding for the MRS, it is essential to first determine the fluence, directionality, and spectrum of the primary and scattered neutrons in the region around the MRS. The codes TART[37] and MCNP were used to simulate the neutron fluence using a model of the OMEGA target bay and target chamber. Measurements of the neutron fluence at various locations in the target bay were conducted with several CR-39 detectors to benchmark the simulations. The resulting data is compared to simulations in Figure 33. Excellent agreement between the data and the simulation is observed, providing confidence in the accuracy of the model. For comparison, the $1/(4\pi R^2)$ curve, which represents the direct primary neutron fluence in the absence of scattering, is shown. The difference between the measured fluence and the $R^{-2}$ curve indicates the level of scattered neutrons at various distances from TCC.

The neutron fluence data, shown in Figure 33, allowed us to optimally design (considering space-constraints) the polyethylene shielding for the MRS that met the engineering requirements. The MCNP model used for this includes the MRS, the OMEGA target chamber, and the OMEGA target bay. A cut through image of the final MRS shielding design is shown in Figure 34(a). This image has been rotated to have the x-axis parallel with the MRS LOS. In addition to the 20 cm thick polyethylene shielding (marked green), a 20 cm thick stainless steel plug was positioned between TCC and the detector to attenuate and moderate unscattered primary neutrons via inelastic scattering.[26] Figure 34(b) shows the simulated neutron fluence per produced neutron in the region around and inside the MRS. As shown by the image, significant attenuation occurs in the magnet return yoke and the shielding in front of the detector. A beam of neutrons passes through the magnet pole gap and can scatter inside the shielding. This is not optimal but unavoidable due to space constraints. The

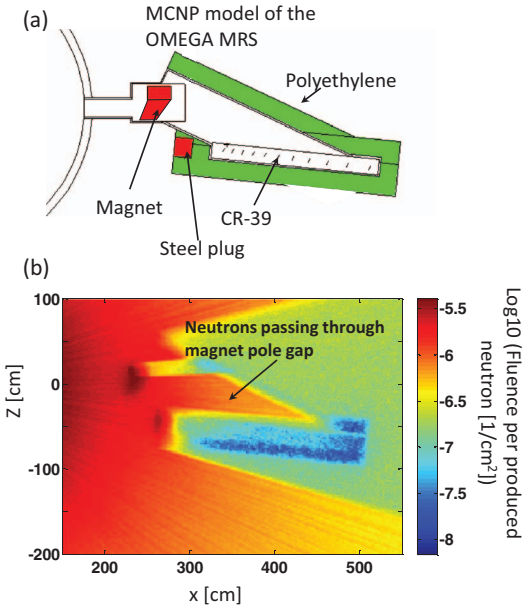


FIG. 34. (a) MCNP model of the OMEGA MRS, which includes the magnet, detector array, 20 cm of polyethylene shielding that surrounds the detector array, and a 20 cm thick piece of stainless steel positioned in front of the detector array to attenuate direct, unscattered primary neutrons via inelastic collisions. (b) Simulated map of neutron fluence per produced neutron in the region around and inside the MRS shielding. The implosion is located at the origin and the MRS LOS is oriented along the x-axis.

fluence of background neutrons around the MRS shielding was simulated and measured to be $\sim 10^{-6}$ n/cm$^2$ per produced primary-neutron (Figure 33). Inside the shielding, the neutron fluence was determined to be $\sim 10^{-7}$ n/cm$^2$ and $\sim 2 \times 10^{-8}$ n/cm$^2$ per produced primary-neutron at the low-energy and high-energy side of the MRS detector, respectively.

An additional check of the simulations and shielding design was conducted by measuring the neutron fluence at the MRS CR-39 detectors before and after the shielding was installed. The results are shown and contrasted to the simulations in Figure 35, which illustrate excellent agreement between measurements and simulations. Having benchmarked the modeling of the OMEGA MRS shielding, a similar

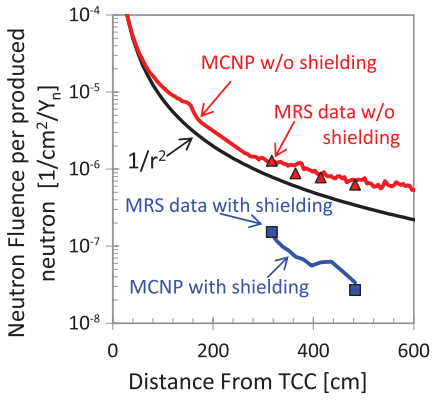


FIG. 35. Measured and simulated neutron fluence (per produced primary-neutron) along the OMEGA MRS detector array with and without shielding around the MRS.

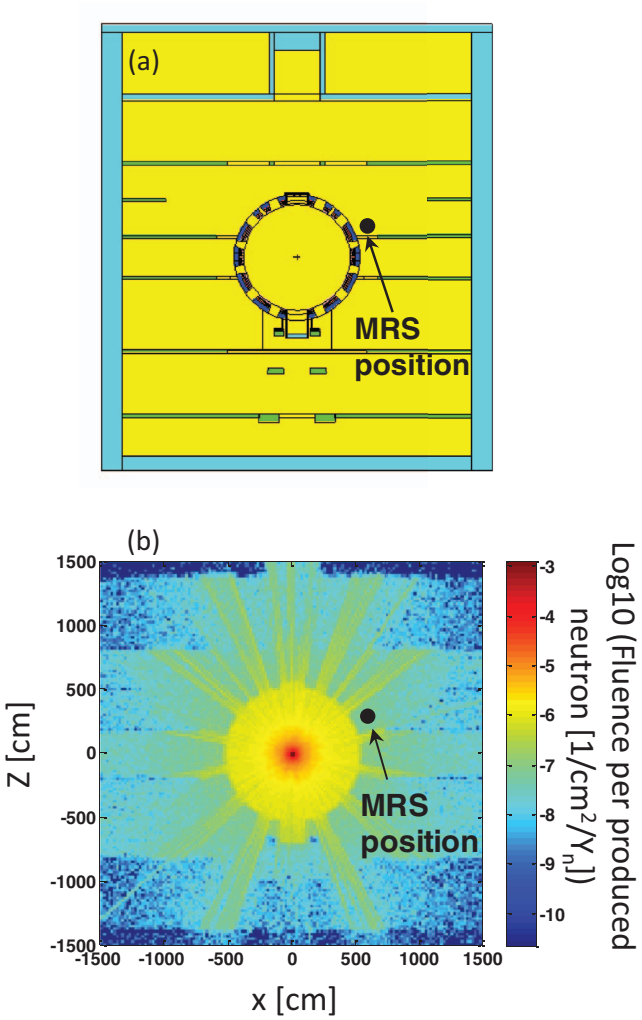


FIG. 36. (a) A detailed MCNP model of the NIF target bay, which includes the NIF target chamber with its laser and diagnostic ports, and the concrete and stainless steel reinforced walls and floors. This model was initially used to determine the neutron fluence at the MRS location. The NIF MRS was subsequently added to the model. (b) Simulated neutron fluence inside the NIF target bay. The fluence is given in neutrons/cm$^2$ per produced neutron. A neutron fluence of $\sim 10^{-7}$ n/cm$^2$ per produced neutron was determined at the MRS location.

modeling could then be applied with high level of confidence to the design of the NIF MRS shielding.

### B. Neutron background characterization and shielding design for the NIF MRS

A detailed MCNP model of the NIF target bay, developed by Lawrence Livermore National Laboratory, was used as a starting point in the effort of optimizing the shielding for the NIF MRS. This model, shown in Figure 36(a),[38] includes a complex representation of the NIF target chamber. In particular, it includes the 10 cm thick spherical aluminum chamber, surrounded by 50 cm of gunite shielding along with the laser and diagnostic ports. The concrete and stainless steel reinforced target-bay walls and floors are also included. Using this model, the fluence of background neutrons was determined to be about $10^{-7}$ neutrons/cm$^2$ per produced primary-neutron at the MRS location, which is close to the chamber equator at

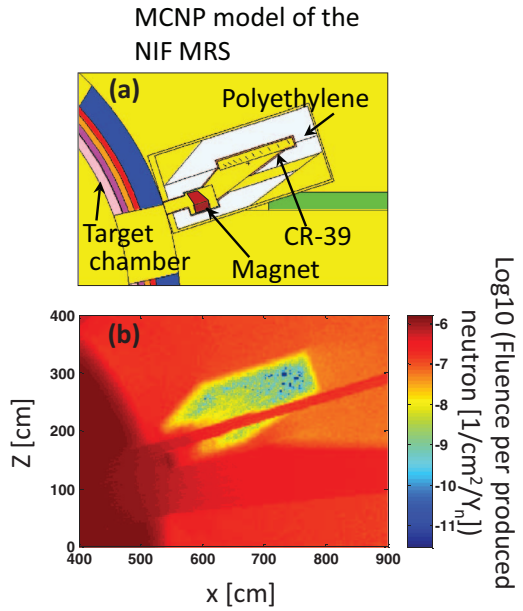


FIG. 37. (a) MCNP model of the final NIF MRS shielding design. (b) Simulated neutron fluence ($\mathrm{Log}_{10}$) around and inside the MRS shielding. The neutron fluence is given in neutrons/cm$^2$ per produced neutron. This simulation shows that the fluence is reduced inside the shielding by about a factor of 50 to $\sim 2 \times 10^{-9}$ n/cm$^2$ per produced neutron.

77°–324° LOS (see Figure 36(b)). As shown by the neutron fluence map, neutrons stream relatively unaffected through the chamber ports. A detailed model of the MRS was incorporated into the NIF target bay model, as shown in Figure 37(a).

A blown-up view of the MRS model with the final shielding design is shown in Figure 37(a). The MRS detector array is located behind the target chamber wall made of 10 cm aluminum and 40 cm of gunite, which provides excellent shielding. The detector array is surrounded by ~40 cm of polyethylene shielding that reduces the fluence of scattered, ambient neutrons. An important feature to the shielding design is the neutron beam dump, which allows the beam of primary, unscattered neutrons to freely pass through the system. MCNP was used to simulate the fluence map of the background neutrons around and inside the MRS shielding (Figure 37(b)). As shown by the map, the simulated neutron background inside the shielding is $\sim 2 \times 10^{-9}$ neutrons/cm$^2$ per produced neutron, indicating that the shielding reduces the neutron fluence ~50 times. This number could not yet be checked experimentally because a neutron yield of a few times $10^{15}$ is required.[25]

## VIII. DIAGNOSING CRYOGENIC DT IMPLOSIONS AT OMEGA AND THE NIF USING THE MRS

Obtaining high compression in ICF requires careful tailoring of the target and laser (or x-ray) drive along with the ability to diagnose the performance of a particular integrated design. The burn averaged $\rho R$, an important performance metric,[12,39,40] is inferred from the DSn spectrum. The absolute neutron spectra and inferred $\rho R$ data obtained with the MRS have been essential for understanding the fuel assembly and for guiding the cryogenic programs at both OMEGA and the NIF to record $\rho R$ values.[12,13,16] Examples of MRS

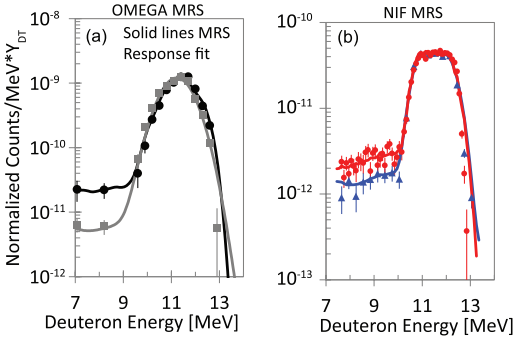


FIG. 38. MRS measured recoil deuteron spectra for two cryogenic DT implosions (shot 55 723 black circles and 54 926 grey squares) on OMEGA (part a) and two cryogenic DT implosions (shot N110608 red circles and N110212 blue triangles) at the NIF (part b). In these experiments, the MRS was operated in low-resolution mode. These spectra are normalized by the primary neutron yield $Y_{DT}$ to directly show the different levels of DSn (and therefore differences in $\rho R$) at deuteron energies <10 MeV corresponding to neutron energies 10–12 MeV (see Figures 29 and 31). The MRS continues to regularly diagnose cryogenic DT implosions at both OMEGA and the NIF. Parts (a) and (b) reprinted with permission from J. A. Frenje *et al.*, Phys. Plasmas **17**, 056311 (2010) and S. H. Glenzer *et al.*, Phys. Plasmas **19**, 056318 (2012), respectively. Copyright 2010 and 2012 American Institute of Physics.

data obtained for two cryogenic DT implosions at OMEGA are shown in Figure 38(a). The MRS characterization and response calculations described in Secs. I–VII are used to interpret the measured MRS recoil deuteron data and infer the emitted ICF neutron spectrum. Described in more detail in other references, the solid lines are best fits to the measured data and provide information about the implosion areal density,[5] the neutron yield,[36] and in some cases ion temperature.[9] These spectra are normalized by the primary neutron yield $Y_{DT}$ to visualize the differences in the DSn energy region. As the relative intensity of the DSn signal is proportional to $\rho R$, the differences between the spectra indicate changes in the observed $\rho R$. Shot 55 723 (black circles) produced the highest $\rho R$ ($295 \pm 44$ mg/cm$^2$)[12,13] yet measured at OMEGA and shot 54 926 (grey squares) is shown ($83 \pm 13$ mg/cm$^2$) for comparison.

The MRS on the NIF plays a critical role in diagnosing cryogenic DT experiments aimed toward achieving thermonuclear ignition and net energy gain. Examples of MRS spectra for two NIF cryogenic DT implosions (N110212 and N110608) are shown in Figure 38(b) and show different observed $\rho Rs$. Again, these recoil spectra are normalized by $Y_{DT}$ to directly show the different DSn levels (and therefore differences in $\rho R$). The inferred $\rho R$ for shots N110212 and N110608 are $570 \pm 50$ mg/cm$^2$ and $910 \pm 50$ mg/cm$^2$, respectively.[15]

## IX. SUMMARY

The ICF neutron spectrum contains essential information about the implosion performance, including areal-density, ion temperature, and neutron yield. These essential implosion parameters are inferred using the MRS, which measures the absolute neutron spectrum between 3 and 30 MeV at OMEGA and 3 and 36 MeV at the NIF. To interpret MRS data, the response function of the system and detector background must be well understood. The Monte Carlo code Geant4 was used to construct the full MRS-response function for various configurations. Validated with commissioning data, these response functions are regularly used to interpret MRS data. The neutron background for the MRS was simulated using the Monte Carlo code MCNP and the results agree well with CR-39 background measurements. Both the OMEGA MRS and NIF MRS are used extensively to accurately diagnose ICF implosions,[5,9,12,13,15,16] and perform high-quality basic science experiments at both facilities.[41–43]

## ACKNOWLEDGMENTS

The authors thank the OMEGA and NIF operations and engineering staff who supported this work. This work was performed under the auspices of the U.S. Department of Energy under Contract No. DE-FG52-09NA29553, NLUF (NA0000877), FSC (Rochester Subaward PO No. 415023-G, UR Account No. 5-24431), LLE (412160-001G), and LLNL (B580243) and by LLNL under DOE Contract No. DE-AC52-07NA27344.

[1]T. R. Boehly, D. L. Brown, R. S. Craxton, R. L. Keck, J. P. Knauer, J. H. Kelly, T. J. Kessler, S. A. Kumpan, S. J. Loucks, S. A. Letzring, F. J. Marshall, R. L. McCrory, S. F. B. Morse, W. Seka, J. M. Soures, and C. P. Verdon, Opt. Commun. **133**(1-6), 495–506 (1997).
[2]E. I. Moses, J. Phys.: Conf. Ser. **112**(1), 012003 (2008).
[3]J. A. Frenje, K. M. Green, D. G. Hicks, C. K. Li, F. H. Seguin, R. D. Petrasso, T. C. Sangster, T. W. Phillips, V. Y. Glebov, D. D. Meyerhofer, S. Roberts, J. M. Soures, C. Stoeckl, K. Fletcher, S. Padalino, and R. J. Leeper, Rev. Sci. Instrum. **72**(1), 854–858 (2001).
[4]F. H. Seguin, J. A. Frenje, C. K. Li, D. G. Hicks, S. Kurebayashi, J. R. Rygg, B. E. Schwartz, R. D. Petrasso, S. Roberts, J. M. Soures, D. D. Meyerhofer, T. C. Sangster, J. P. Knauer, C. Sorce, V. Y. Glebov, C. Stoeckl, T. W. Phillips, R. J. Leeper, K. Fletcher, and S. Padalino, Rev. Sci. Instrum. **74**(2), 975–995 (2003).
[5]J. A. Frenje, D. T. Casey, C. K. Li, F. H. Seguin, R. D. Petrasso, V. Y. Glebov, P. B. Radha, T. C. Sangster, D. D. Meyerhofer, S. P. Hatchett, S. W. Haan, C. J. Cerjan, O. L. Landen, K. A. Fletcher, and R. J. Leeper, Phys. Plasmas **17**, 056311 (2010).
[6]S. Agostinelli, J. Allison, K. Amako, J. Apostolakis, H. Araujo, P. Arce, M. Asai, D. Axen, S. Banerjee, G. Barrand, F. Behner, L. Bellagamba, J. Boudreau, L. Broglia, A. Brunengo, H. Burkhardt, S. Chauvie, J. Chuma, R. Chytracek, G. Cooperman, G. Cosmo, P. Degtyarenko, A. Dell'Acqua, G. Depaola, D. Dietrich, R. Enami, A. Feliciello, C. Ferguson, H. Fesefeldt, G. Folger, F. Foppiano, A. Forti, S. Garelli, S. Giani, R. Giannitrapani, D. Gibin, J. J. G. Cadenas, I. González, G. G. Abril, G. Greeniaus, W. Greiner, V. Grichine, A. Grossheim, S. Guatelli, P. Gumplinger, R. Hamatsu, K. Hashimoto, H. Hasui, A. Heikkinen, A. Howard, V. Ivanchenko, A. Johnson, F. W. Jones, J. Kallenbach, N. Kanaya, M. Kawabata, Y. Kawabata, M. Kawaguti, S. Kelner, P. Kent, A. Kimura, T. Kodama, R. Kokoulin, M. Kossov, H. Kurashige, E. Lamanna, T. Lampén, V. Lara, V. Lefebure, F. Lei, M. Liendl, W. Lockman, F. Longo, S. Magni, M. Maire, E. Medernach, K. Minamimoto, P. Mora de Freitas, Y. Morita, K. Murakami, M. Nagamatu, R. Nartallo, P. Nieminen, T. Nishimura, K. Ohtsubo, M. Okamura, S. O'Neale, Y. Oohata, K. Paech, J. Perl, A. Pfeiffer, M. G. Pia, F. Ranjard, A. Rybin, S. Sadilov, E. Di Salvo, G. Santin, T. Sasaki, N. Savvas, Y. Sawada, S. Scherer, S. Sei, V. Sirotenko, D. Smith, N. Starkov, H. Stoecker, J. Sulkimo, M. Takahata, S. Tanaka, E. Tcherniaev, E. S. Tehrani, M. Tropeano, P. Truscott, H. Uno, L. Urban, P. Urban, M. Verderi, A. Walkden, W. Wander, H. Weber, J. P. Wellisch, T. Wenaus, D. C. Williams, D. Wright, T. Yamada, H. Yoshida, and D. Zschiesche, Nucl. Instrum. Methods Phys. Res. A **506**(3), 250–303 (2003).
[7]J. Källne and H. Enge, Nucl. Instrum. Methods Phys. Res. A **311**(3), 595–602 (1992).
[8]J. A. Frenje, D. T. Casey, C. K. Li, J. R. Rygg, F. H. Seguin, R. D. Petrasso, V. Y. Glebov, D. D. Meyerhofer, T. C. Sangster, S. Hatchett, S. Haan, C. Cerjan, O. Landen, M. Moran, P. Song, D. C. Wilson, and R. J. Leeper, Rev. Sci. Instrum. **79**(10), 10E502 (2008).

[9]M. G. Johnson, J. A. Frenje, D. T. Casey, C. K. Li, F. H. Seguin, R. Petrasso, R. Ashabranner, R. M. Bionta, D. L. Bleuel, E. J. Bond, J. A. Caggiano, A. Carpenter, C. J. Cerjan, T. J. Clancy, T. Doeppner, M. J. Eckart, M. J. Edwards, S. Friedrich, S. H. Glenzer, S. W. Haan, E. P. Hartouni, R. Hatarik, S. P. Hatchett, O. S. Jones, G. Kyrala, S. L. Pape, R. A. Lerche, O. L. Landen, T. Ma, A. J. MacKinnon, M. A. McKernan, M. J. Moran, E. Moses, D. H. Munro, J. McNaney, H. S. Park, J. Ralph, B. Remington, J. R. Rygg, S. M. Sepke, V. Smalyuk, B. Spears, P. T. Springer, C. B. Yeamans, M. Farrell, D. Jasion, J. D. Kilkenny, A. Nikroo, R. Paguio, J. P. Knauer, V. Y. Glebov, T. C. Sangster, R. Betti, C. Stoeckl, J. Magoon, M. J. Shoup III, G. P. Grim, J. Kline, G. L. Morgan, T. J. Murphy, R. J. Leeper, C. L. Ruiz, G. W. Cooper, and A. J. Nelson, Rev. Sci. Instrum. **83**(10), 10D308 (2012).

[10]D. T. Casey, Ph.D. dissertation, MIT, 2012.

[11]J. A. Frenje, C. K. Li, F. H. Seguin, D. T. Casey, R. D. Petrasso, T. C. Sangster, R. Betti, V. Y. Glebov, and D. D. Meyerhofer, Phys. Plasmas **16**(4), 042704 (2009).

[12]T. C. Sangster, V. N. Goncharov, R. Betti, T. R. Boehly, D. T. Casey, T. J. B. Collins, R. S. Craxton, J. A. Delettrez, D. H. Edgell, R. Epstein, K. A. Fletcher, J. A. Frenje, Y. Y. Glebov, D. R. Harding, S. X. Hu, I. V. Igumenschev, J. P. Knauer, S. J. Loucks, C. K. Li, J. A. Marozas, F. J. Marshall, R. L. McCrory, P. W. McKenty, D. D. Meyerhofer, P. M. Nilson, S. P. Padalino, R. D. Petrasso, P. B. Radha, S. P. Regan, F. H. Seguin, W. Seka, R. W. Short, D. Shvarts, S. Skupsky, V. A. Smalyuk, J. M. Soures, C. Stoeckl, W. Theobald, and B. Yaakobi, Phys. Plasmas **17**, 056312 (2010).

[13]V. N. Goncharov, T. C. Sangster, T. R. Boehly, S. X. Hu, I. V. Igumenshchev, F. J. Marshall, R. L. McCrory, D. D. Meyerhofer, P. B. Radha, W. Seka, S. Skupsky, C. Stoeckl, D. T. Casey, J. A. Frenje, and R. D. Petrasso, Phys. Rev. Lett. **104**(16), 165001 (2010).

[14]C. J. Forrest, P. B. Radha, V. Y. Glebov, V. N. Goncharov, J. P. Knauer, A. Pruyne, M. Romanofsky, T. C. Sangster, M. J. Shoup III, C. Stoeckl, D. T. Casey, M. Gatu-Johnson, and S. Gardner, Rev. Sci. Instrum. **83**(10), 10D919 (2012).

[15]S. H. Glenzer, D. A. Callahan, A. J. MacKinnon, J. L. Kline, G. Grim, E. T. Alger, R. L. Berger, L. A. Bernstein, R. Betti, D. L. Bleuel, T. R. Boehly, D. K. Bradley, S. C. Burkhart, R. Burr, J. A. Caggiano, C. Castro, D. T. Casey, C. Choate, D. S. Clark, P. Celliers, C. J. Cerjan, G. W. Collins, E. L. Dewald, P. DiNicola, J. M. DiNicola, L. Divol, S. Dixit, T. Doppner, R. Dylla-Spears, E. Dzenitis, M. Eckart, G. Erbert, D. Farley, J. Fair, D. Fittinghoff, M. Frank, L. J. A. Frenje, S. Friedrich, M. G. Johnson, C. Gibson, E. Giraldez, V. Glebov, S. Glenn, N. Guler, S. W. Haan, B. J. Haid, B. A. Hammel, A. V. Hamza, C. A. Haynam, G. M. Heestand, M. Hermann, H. W. Hermann, D. G. Hicks, D. E. Hinkel, J. P. Holder, D. M. Holunda, J. B. Horner, W. W. Hsing, H. Huang, N. Izumi, M. Jackson, O. S. Jones, D. H. Kalantar, R. Kauffman, J. D. Kilkenny, R. K. Kirkwood, J. Klingmann, T. Kohut, J. P. Knauer, J. A. Koch, B. Kozioziemki, G. A. Kyrala, A. L. Kritcher, J. Kroll, K. L. Fortune, L. Lagin, O. L. Landen, D. W. Larson, D. LaTray, R. J. Leeper, S. L. Pape, J. D. Lindl, R. Lowe-Webb, T. Ma, J. McNaney, A. G. MacPhee, T. N. Malsbury, E. Mapoles, C. D. Marshall, N. B. Meezan, F. Merrill, P. Michel, J. D. Moody, A. S. Moore, M. Moran, K. A. Moreno, D. H. Munro, B. R. Nathan, A. Nikroo, R. E. Olson, C. D. Orth, A. E. Pak, P. K. Patel, T. Parham, R. Petrasso, J. E. Ralph, H. Rinderknecht, S. P. Regan, H. F. Robey, J. S. Ross, M. D. Rosen, R. Sacks, J. D. Salmonson, R. Saunders, J. Sater, C. Sangster, M. B. Schneider, F. H. Seguin, M. J. Shaw, B. K. Spears, P. T. Springer, W. Stoeffl, L. J. Suter, C. A. Thomas, R. Tommasini, R. P. J. Town, C. Walters, S. Weaver, S. V. Weber, P. J. Wegner, P. K. Whitman, K. Widmann, C. C. Widmayer, C. H. Wilde, D. C. Wilson, B. V. Wonterghem, B. J. MacGowan, L. J. Atherton, M. J. Edwards, and E. I. Moses, Phys. Plasmas **19**(5), 056318 (2012).

[16]A. J. Mackinnon, J. L. Kline, S. N. Dixit, S. H. Glenzer, M. J. Edwards, D. A. Callahan, N. B. Meezan, S. W. Haan, J. D. Kilkenny, T. Döppner, D. R. Farley, J. D. Moody, J. E. Ralph, B. J. MacGowan, O. L. Landen, H. F. Robey, T. R. Boehly, P. M. Celliers, J. H. Eggert, K. Krauter, G. Frieders, G. F. Ross, D. G. Hicks, R. E. Olson, S. V. Weber, B. K. Spears, J. D. Salmonsen, P. Michel, L. Divol, B. Hammel, C. A. Thomas, D. S. Clark, O. S. Jones, P. T. Springer, C. J. Cerjan, G. W. Collins, V. Y. Glebov, J. P. Knauer, C. Sangster, C. Stoeckl, P. McKenty, J. M. McNaney, R. J. Leeper, C. L. Ruiz, G. W. Cooper, A. G. Nelson, G. G. A. Chandler, K. D. Hahn, M. J. Moran, M. B. Schneider, N. E. Palmer, R. M. Bionta, E. P. Hartouni, S. LePape, P. K. Patel, N. Izumi, R. Tommasini, E. J. Bond, J. A. Caggiano, R. Hatarik, G. P. Grim, F. E. Merrill, D. N. Fittinghoff, N. Guler, O. Drury, D. C. Wilson, H. W. Herrmann, W. Stoeffl, D. T. Casey, M. G. Johnson, J. A. Frenje, R. D. Petrasso, A. Zylestra, H. Rinderknecht, D. H. Kalantar, J. M. Dzenitis, P. Di Nicola, D. C. Eder, W. H. Courdin, G. Gururangan, S. C. Burkhart, S. Friedrich, D. L. Blueuel, L. A. Bernstein, M. J. Eckart, D. H. Munro, S. P. Hatchett, A. G. Macphee, D. H. Edgell, D. K. Bradley, P. M. Bell, S. M. Glenn, N. Simanovskaia, M. A. Barrios, R. Benedetti, G. A. Kyrala, R. P. J. Town, E. L. Dewald, J. L. Milovich, K. Widmann, A. S. Moore, G. LaCaille, S. P. Regan, L. J. Suter, B. Felker, R. C. Ashabranner, M. C. Jackson, R. Prasad, M. J. Richardson, T. R. Kohut, P. S. Datte, G. W. Krauter, J. J. Klingman, R. F. Burr, T. A. Land, M. R. Hermann, D. A. Latray, R. L. Saunders, S. Weaver, S. J. Cohen, L. Berzins, S. G. Brass, E. S. Palma, R. R. Lowe-Webb, G. N. McHalle, P. A. Arnold, L. J. Lagin, C. D. Marshall, G. K. Brunton, D. G. Mathisen, R. D. Wood, J. R. Cox, R. B. Ehrlich, K. M. Knittel, M. W. Bowers, R. A. Zacharias, B. K. Young, J. P. Holder, J. R. Kimbrough, T. Ma, K. N. La Fortune, C. C. Widmayer, M. J. Shaw, G. V. Erbert, K. S. Jancaitis, J. M. DiNicola, C. Orth, G. Heestand, R. Kirkwood, C. Haynam, P. J. Wegner, P. K. Whitman, A. Hamza, E. G. Dzenitis, R. J. Wallace, S. D. Bhandarkar, T. G. Parham, R. Dylla-Spears, E. R. Mapoles, B. J. Kozioziemski, J. D. Sater, C. F. Walters, B. J. Haid, J. Fair, A. Nikroo, E. Giraldez, K. Moreno, B. Vanwonterghem, R. L. Kauffman, S. Batha, D. W. Larson, R. J. Fortner, D. H. Schneider, J. D. Lindl, R. W. Patterson, L. J. Atherton, and E. I. Moses, Phys. Rev. Lett. **108**(21), 215005 (2012).

[17]X-5 Monte Carlo Team, "MCNP- A General Monte Carlo N-Particle Transport Code, Version 5," Los Alamos National Laboratory, Report No. LA-UR-03-1987, 2005.

[18]"MCNPX User's Manual, Version 2.6.0," Los Alamos National Laboratory Report, Report No. LA-CP-07-1473, 2007.

[19]Dexter Magnetic Technologies, Inc., 400 Karin Lane, Hicksville, NY 11801, USA.

[20]M. Devine, personal communication (2006).

[21]Track Analysis Systems Ltd., H. H. Wills Physics Lab., Tyndall Ave., Bristol BS8 1TL, United Kingdom.

[22]D. G. Hicks, Massachusetts Institute of Technology Thesis, 1999.

[23]D. T. Casey, J. A. Frenje, F. H. Séguin, C. K. Li, M. J. Rosenberg, H. Rinderknecht, M. J.-E. Manuel, M. G. Johnson, J. C. Schaeffer, R. Frankel, N. Sinenian, R. A. Childs, R. D. Petrasso, V. Y. Glebov, T. C. Sangster, M. Burke, and S. Roberts, Rev. Sci. Instrum. **82**(7), 073502 (2011).

[24]J. Frenje, personal communication (2013).

[25]J. A. Frenje, C. K. Li, F. H. Seguin, D. G. Hicks, S. Kurebayashi, R. D. Petrasso, S. Roberts, V. Y. Glebov, D. D. Meyerhofer, T. C. Sangster, J. M. Soures, C. Stoeckl, C. Chiritescu, G. J. Schmid, and R. A. Lerche, Rev. Sci. Instrum. **73**(7), 2597–2605 (2002).

[26]E. M. Lent, Report No. LLNL UCRL-50857, 1970.

[27]ISOTEC Inc., 3050 Spruce St., St. Louis, MO 6310.

[28]K. Fletcher, "Deuterated polyethylene film preparation—Comparing two methods" (unpublished).

[29]General Atomics LLC, 3550 General Atomics Court, San Diego, CA 92121-1122.

[30]J. Mark, *Physical Properties of Polymers Handbook* (Springer, 2006).

[31]M. B. Chadwick, P. Oblozinský, M. Herman, N. M. Greene, R. D. McKnight, D. L. Smith, P. G. Young, R. E. MacFarlane, G. M. Hale, S. C. Frankle, A. C. Kahler, T. Kawano, R. C. Little, D. G. Madland, P. Moller, R. D. Mosteller, P. R. Page, P. Talou, H. Trellue, M. C. White, W. B. Wilson, R. Arcilla, C. L. Dunford, S. F. Mughabghab, B. Pritychenko, D. Rochman, A. A. Sonzogni, C. R. Lubitz, T. H. Trumbull, J. P. Weinman, D. A. Brown, D. E. Cullen, D. P. Heinrichs, D. P. McNabb, H. Derrien, M. E. Dunn, N. M. Larson, L. C. Leal, A. D. Carlson, R. C. Block, J. B. Briggs, E. T. Cheng, H. C. Huria, M. L. Zerkle, K. S. Kozier, A. Courcelle, V. Pronyaev, and S. C. van der Marck, Nucl. Data Sheets **107**(12), 2931–3060 (2006).

[32]F. B. Brown, R. F. Barrett, T. E. Booth, J. S. Bull, L. J. Cox, R. A. Forster, T. J. Goorley, R. D. Mosteller, S. E. Post, R. E. Prael, E. C. Selcow, A. Sood, and J. Sweezy, Trans. Am. Nucl. Soc. **87**, 273 (2002).

[33]J. Frenje, personal communication (2007).

[34]D. G. Hicks, C. K. Li, F. H. Seguin, A. K. Ram, J. A. Frenje, R. D. Petrasso, J. M. Soures, V. Y. Glebov, D. D. Meyerhofer, S. Roberts, C. Sorce, C. Stockl, T. C. Sangster, and T. W. Phillips, Phys. Plasmas **7**(12), 5106–5117 (2000).

[35]V. Y. Glebov, C. Stoeckl, T. C. Sangster, S. Roberts, G. J. Schmid, R. A. Lerche, and M. J. Moran, Rev. Sci. Instrum. **75**(10), 3559–3562 (2004).

[36]D. T. Casey, J. A. Frenje, M. G. Johnson, F. H. Seguin, C. K. Li, R. D. Petrasso, V. Y. Glebov, J. Katz, J. P. Knauer, D. D. Meyerhofer, T. C. Sangster, R. M. Bionta, D. L. Bleuel, T. Doppner, S. Glenzer, E. Hartouni, S. P. Hatchett, S. L. Pape, T. Ma, A. MacKinnon, M. A. McKernan, M. Moran, E. Moses, H.-S. Park, J. Ralph, B. A. Remington, V. Smalyuk, C. B. Yeamans, J. Kline, G. Kyrala, G. A. Chandler, R. J. Leeper, C. L. Ruiz,

G. W. Cooper, A. J. Nelson, K. Fletcher, J. Kilkenny, M. Farrell, D. Jasion, and R. Paguio, Rev. Sci. Instrum. **83**(10), 10D912 (2012).
[37]D. E. Cullen, LLNL, UCRL-ID-126455, 2003.
[38]H. Khater, personal communication (2008).
[39]R. Betti, P. Y. Chang, B. K. Spears, K. S. Anderson, J. Edwards, M. Fatenejad, J. D. Lindl, R. L. McCrory, R. Nora, and D. Shvarts, Phys. Plasmas **17**(5), 058102 (2010).
[40]J. D. Lindl, *Inertial Confinement Fusion: The Quest for Ignition and Energy Gain using Indirect Drive* (Springer, New York, 1998).
[41]J. A. Frenje, C. K. Li, F. H. Seguin, D. T. Casey, R. D. Petrasso, D. P. McNabb, P. Navratil, S. Quaglioni, T. C. Sangster, V. Y. Glebov, and D. D. Meyerhofer, Phys. Rev. Lett. **107**(12), 122502 (2011).
[42]D. T. Casey, J. A. Frenje, M. G. Johnson, M. J. E. Manuel, N. Sinenian, A. B. Zylstra, F. H. Séguin, C. K. Li, R. D. Petrasso, V. Y. Glebov, P. B. Radha, D. D. Meyerhofer, T. C. Sangster, D. P. McNabb, P. A. Amendt, R. N. Boyd, S. P. Hatchett, S. Quaglioni, J. R. Rygg, I. J. Thompson, A. D. Bacher, H. W. Herrmann, and Y. H. Kim, Phys. Rev. Lett. **109**(2), 025003 (2012).
[43]D. T. Casey, J. A. Frenje, M. G. Johnson, M. J. E. Manuel, H. G. Rinderknecht, N. Sinenian, F. H. Séguin, C. K. Li, R. D. Petrasso, P. B. Radha, J. A. Delettrez, V. Y. Glebov, D. D. Meyerhofer, T. C. Sangster, D. P. McNabb, P. A. Amendt, R. N. Boyd, J. R. Rygg, H. W. Herrmann, Y. H. Kim, and A. D. Bacher, Phys. Rev. Lett. **108**(7), 075002 (2012).